



저작자표시-비영리-변경금지 2.0 대한민국

이용자는 아래의 조건을 따르는 경우에 한하여 자유롭게

- 이 저작물을 복제, 배포, 전송, 전시, 공연 및 방송할 수 있습니다.

다음과 같은 조건을 따라야 합니다:



저작자표시. 귀하는 원저작자를 표시하여야 합니다.



비영리. 귀하는 이 저작물을 영리 목적으로 이용할 수 없습니다.



변경금지. 귀하는 이 저작물을 개작, 변형 또는 가공할 수 없습니다.

- 귀하는, 이 저작물의 재이용이나 배포의 경우, 이 저작물에 적용된 이용허락조건을 명확하게 나타내어야 합니다.
- 저작권자로부터 별도의 허가를 받으면 이러한 조건들은 적용되지 않습니다.

저작권법에 따른 이용자의 권리는 위의 내용에 의하여 영향을 받지 않습니다.

이것은 [이용허락규약\(Legal Code\)](#)을 이해하기 쉽게 요약한 것입니다.

[Disclaimer](#)

Ph. D. DISSERTATION

Experimental Investigation of Electrokinetic
Response near Perm-selective Membrane
with Microstructures

마이크로 구조물에 의한 이온 선택성 투과막 근처
전기동역학 변화의 실험적 검증

BY

KEON HUH

AUGUST 2019

DEPARTMENT OF
ELECTRICAL AND COMPUTER ENGINEERING
COLLEGE OF ENGINEERING
SEOUL NATIONAL UNIVERSITY

Abstract

KEON HUH

DEPARTMENT OF
ELECTRICAL AND COMPUTER ENGINEERING
COLLEGE OF ENGINEERING
SEOUL NATIONAL UNIVERSITY

Ion perm-selectivity have been one of the unique properties in nanofluidic channels. Compared to the nanochannel thickness, the Debye layer length thickness is non-negligible and therefore the electrical double layer overlap inside the nanochannel under certain conditions. As the voltage is applied through the micro-nanochannel (i.e. thinner than O (100) nm), a phenomenon called Ion concentration polarization(ICP) appears. The mechanism of ICP is that only counter-ions can pass through a charged nanoporous membrane under dc bias[1, 2] therefore creates an imbalance of ion concentrations at anodic and cathodic side of the membrane. The region with low concentration is called the ion depletion zone and region with high concentration is called ion enrichment zone[1, 2]. Ion distribution caused by ICP of the depletion zone can be classified into 2 regions; outside of the depletion zone and inside the depletion zone. Inside the ion depletion zone, various fundamental issues have been studied, such as electroosmotic instability, overlimiting current, and so on.

Outside the depletion zone, purification/desalination/preconcentration applications by the continuous extraction of fluid have drawn significant attention.

In this thesis, we experimentally investigated the electrokinetic responses inside and outside of the depletion zone during ICP phenomena by changing the geometry structure of the microchannel and also by installing microstructures inside the depletion zone. To verify the electrokinetic responses, concentration profile, particle tracking, and the electrical response were investigated as well. The chapters are divided into 4 chapters.

First in chapter 2, a multilayer micro/nanofluidic device for selective preconcentration and online collection of charged molecules with different physicochemical properties based on ion concentration polarization was proposed. With the balance of electroosmotic drag force and electrophoretic force on the molecules, they could be highly preconcentrated and separated simultaneously. With the design of repeated microchamber structure, ion depletion zone was stabilized and plugs were well-defined. For subsequent on-chip or off-chip application, pneumatic microvalve system was integrated and selectively preconcentrated. Alexa dye was collected from the original sample mixture of Sulforhodamine B and Alexa Fluor 488 without further diffusion or dispersion.

Secondly in chapter 3, the electrokinetic effect[1, 3, 4] of the micro dielectric pillars in a micro confined environment by multi-physics simulations and micro/nanofluidic experiments was proposed. While dielectric microstructures in a macroscale system consisted of a perm-selective

membrane has negative influences on a perm-selective ion transportation due to current shadow effects, the structure can promote the transportation in a microscale confined system because the major driving mechanisms of the ion transportation are transitioned from electro-convective instability (EOI) to surface conduction (SC) and electroosmotic flow (EOF). In this chapter, we provide rigorous evidences how SC and EOF around the dielectric microstructures can accelerate the ion transportation by multi-physics simulations and direct visualizations. Additional ion enrichment zones (AIEZ) are formed on each microstructure inside an ion depletion zone so that AIEZs can directly bridge ion carriers from bulk to the nanoporous membrane. Furthermore, we verify that the physical configuration of a micropillar array has a critical impact on SC and EOF, which has been typically neglected. While vortical flow by EOF is isolated in staggered pillar configuration, the vortices are connected in the aligned pillar configuration so that the latter configuration has higher ion transport efficiency, leading to higher overlimiting current (OLC).

Thirdly in chapter 4, an experimental and multi-physical simulation of ion transport enhancement in macroscale system by employing different spacer structures inside the ion depletion zone was proposed. By I-V characterization and imaging of the concentration profiles with spacers in two different patterns, we found that by organizing the spacers in different manners, specific patterned spacers can enhance the charge transport in the unstable electro-osmotic instability dominant regime by suppressing the electro-osmotic instability in systems where it is unwanted and by fixing the electroconvective mixing in each desired location. By properly patterned configuration, we can regularize

the electroconvection and were able to enhance the electroconvective mixing efficiency. Therefore, the significant enhance of the net transport led to the increase of the OLC.

In the Appendix, as there was no relevance to this thesis topic Appendix A was excluded from the main chapters. In Appendix A, by employing laminar flow characteristics, anisotropic attachment of *S. typhimurium* flagellated bacteria to the microparticles were demonstrated for a chemotactic delivery. Controlling flows upwardly/downwardly enabled an anisotropic attachment of the bacteria. Direct visualizations using fluorescent intensity and SEM imaging were performed for the attachment. Appendix B and C are numerical simulations which support Chapter 2 and Chapter 3 individually.

Keywords: Micro/Nanofluid, Electrokinetics, Permselective Ion Transport, Ion Concentration Polarization (ICP), Overlimiting current (OLC), Preconcentration, Dielectric pillar, Spacer

Student Number: 2013-23145

Contents

Abstract	i
Contents	vii
List of Figures	ix
Chapter 1. Introduction	1
1.1 Electrical double layer	1
1.1.1 Electrical double layer	1
1.1.2 Permselective ion transport	4
1.2 Ion concentration polarization (ICP)	5
1.3 I-V characteristic in an ion-exchange membrane	6
1.4 Definitions of terms	8
1.5 Thesis outline	8
Chapter 2. Selective Preconcentration and Collection of Two Charged Molecules in Microchannels ...	12
2.1 Introduction	15
2.2 Experimental setup	18
2.3 Device operation	21
2.3.1 ICP operation	21

2.3.2 Pneumatic microvalve operation	22
2.4. Results and discussion	24
2.4.1 Selective preconcentration	24
2.4.2 Stabilization of selective preconcentration	27
2.4.3 Quantitative analysis for separation and preconcentration efficiency	28
2.4.4 Isolation of preconcentrated plugs by pneumatic microvalve system	31
2.4.5 Collection of preconcentrated plugs by pneumatic microvalve system	22
2.5. Conclusions	36

Chapter 3. Surface Conduction and Electroosmotic Flow

Contribution on Perm-Selective Ion Transport

.....	37
3.1 Introduction	37
3.2 Experimental setups	41
3.3 Results and discussion	44
3.3.1 Dielectric pillars inside the ion depletion zone	44
3.3.2 Electrokinetic effects of charged dielectric pillar at SC and EOF regime	46
3.3.3 SC and EOF in staggered dielectric pillar configuration	48

3.3.4 Current-voltage characteristics depending on surface charge density and Debye length of the staggered configuration	51
3.3.5 SC and EOF in aligned dielectric pillar configuration	53
3.3.6 Current-voltage characteristics depending on surface charge density and Debye length of the aligned configuration	55
3.3.7 OLC enhancement by the dielectric pillar	57
3.4. Conclusions	59

Chapter 4. Electroosmotic Instability Contribution

on Perm-Selective Ion Transport..... 61

4.1 Introduction	61
4.2 Experimental setups.....	64
4.3 Results and discussion	67
4.3.1 Concentration profile of spacer array configuration.....	67
4.3.2 Current-Voltage characteristic of spacer configuration	70
4.3.3 Surface charge of spacer configuration	72
4.4 Conclusions	74

Chapter 5. Conclusions..... 75

Appendix 77

A. Laminar flow assisted anisotropic bacteria absorption for chemotaxis delivery	77
B. Numerical analysis of ICP layer for straight and repeated chamber structure	95
C. Governing equations and boundary conditions for dielectric pillars inside the ICP layer	98
Reference.....	103
Abstract in Korean (국문 요약)	111

List of Figures

Figure 1.1 The schematic representation of the electrical double layer. The surface is negatively charged. The Stern layer and Gouy-Chapman layer together form the electrical double layer (EDL). 2

Figure 1.2 (a) Schematic diagram of ion concentration distribution of a cation perm-selective nanostructure which only lets cations pass through. N^+ and N^- are the fluxes of cation and anion, respectively, and the subscripts *diff* and *drift* represent the diffusive and drift ion transport, respectively..... 5

Figure 1.3 The schematic representation of the behavior of a current in a system where there is an electric field applied over a stream of electrolyte is divided by a charge selective interface. The three regions ohmic, limiting and overlimiting can be recognized. 7

Figure 2.2 (a) Microscopic view of the selective preconcentration device. The microchannels in the ICP layer are indicated with blue ink and the microchannels in the valve layer are indicated red. (b) An exploded view of the device with (i) a valve layer, (ii) an ICP layer and (iii) a Nafion patterned slide glass. (c) Assembled multilayered online selective preconcentration device. 17

Figure 2.3.2 Microscopic images of 3-step valve control sequence: Step1 – ICP

preconcentration to form a high concentration plug, Step2 – isolation of a highly preconcentrated plug at specific chamber, and Step3 – collection of the highly preconcentrated plug into upward channel..... 20

Figure 2.4.1 (a) Time-lapse images of selective preconcentration of SRB and Alexa. High concentration ratio is represented by the brightness of fluorescence. Since the physicochemical properties of two dyes were different, they were preconcentrated at different locations. (b) Schematic diagram of selective preconcentration mechanism with different mobility. The separation was drawn by the equilibrium between electroosmotic drag force and electrophoretic force exerted on molecules. 21

Figure 2.4.3 (a) Overall fluorescence intensity tracked in each chamber as a function of time. The concentration ratio of selectively preconcentrated Alexa in chamber 3 exceeded 100-fold, maintaining the preconcentration factor high enough in repeated valve operations. (b) Red/green color profile in chamber 3, showing the chamber 3 only has Alexa. (c) Red/green color profile in chamber 1, showing the chamber 1 only has SRB. Fluctuations after 30 minutes in all plots are due to microvalve operations. 23

Figure 2.4.4 Time-lapse images showing the dispersion of isolated plug when the valves are (A) OFF and (B) ON 25

Figure 2.4.5 (a) Snapshots of repeated valve operations collecting selectively

preconcentrated plugs. Compared to the initial state, the measurement window was being filled with green dye (Alexa) over several valve operations. (b) Average intensity change in the measurement window over number of repetition of valve operations. The average intensity exceeded 10-fold in a single valve operation, and 30-fold after nine operations. Note that there was no SRB in the measurement window..... 32

Figure 3.1 (a) Preliminary experimental current-voltage characteristics of micro/nanofluidic device with and without micropillar. (b) Schematic diagram of two mechanisms of perm-selective ion transportation; (i) surface-driven electroosmosis and (ii) surface conduction through electrical double layer on the dielectric pillar.34

Figure 3.2 (a) Snapshot and (b) microscopic images of fabricated micro/nanofluidic device, integrated with the dielectric pillars on anodic side.37

Figure 3.3.1 Experimentally measured OLC depending on the number of pillar array.40

Figure 3.3.3 (a) Numerically simulated and (b) experimental visualized deformed concentration profile of the staggered dielectric pillar configuration. The numerically obtained concentration profile is normalized by bulk concentration c_0 . (c) and (d) are the flow field simulation and flow tracking

experimental results of the staggered configuration, respectively.....45

Figure 3.3.4 Current-voltage characteristics depending on surface charge density and Debye length of the staggered configuration. In these tile plots, q_s is the surface charge density of dielectric spacer, F is the Faraday constant, a is the radius of the dielectric spacer and λ_D is the Debye length. The denoted surface charge density and the Debye length are dimensionless. In each plot, current density and applied voltage are normalized by limiting current scale $i_0 = 2FDc_0 / L$ and thermal voltage scale, respectively.....53

Figure 3.3.5 (a) Numerically simulated and (b) experimental visualized deformed concentration profile of the aligned dielectric pillar configuration. (c) and (d) are the flow field simulation and flow tracking experimental results of aligned configuration, respectively.....59

Figure 3.3.6 Current-voltage characteristics depending on surface charge density and Debye length of the aligned configuration.....64

Figure 3.3.7 Experimentally measured current-voltage relations for no pillar (rectangle), staggered (triangle) and aligned configuration (circle).....64

Figure 4.1 (a) Schematic diagram of electro-convective instability (EOI) and the schematic of deformed convection by spacer. (b) Pre-experimentally measured current-voltage relations for no spacer (triangle-yellow) and staggered spacer (square-blue).....66

Figure 4.2 (a) Fabrication step of micro/nanofluidic device using Nafion PFSA membrane sheet. (b) Snapshot and microscopic images of fabricated micro/nanofluidic device, integrated with spacer array on anodic side 71

Figure 4.3.1 (a) Experimental visualized and numerically simulated concentration profile of no spacer configuration. (b) and (c) are experimental visualized and numerically simulated concentration profile of staggered and aligned spacer configuration..... 75

Figure 4.3.2 (a) Simulated results of current-time characteristic of no spacer (gray), staggered (blue) and aligned configuration (red). (b) Experimentally measured current-voltage relations for no spacer (triangle-gray), staggered (rectangular-blue) and aligned configuration (circle-red). 79

Figure 4.3.3 (a) Experimentally measured current-voltage relations for no spacer (triangle-gray), staggered (rectangular-blue) and aligned configuration (circle-red); Color not filled indicate BSA coating was applied to the device. (b) Table of overlimiting current (OLC) value of Figure 4.3.3 (a). (c) Simulated results of current density depending on surface charge density of spacer..... 81

Appendix Figure A.3 Adsorption concept for anisotropic bacteria attachment 83

Appendix Figure A.4 (a) Fabricated device, (b) microscopic image of the

trapper array, (c) magnified view for 50 um microcube trapping and (d) SEM image of the trapper. Horizontal (dh), vertical (dv) distances and height of trapper were varied depending on the size of microcubes, while the dimension of trapper itself was fixed 83

Appendix Figure A.4.1 Numerically simulated streamlines and velocity magnitude contour plots of (a) before and (b) after capturing microcubes. Reynolds number was set to be 1. The velocity has the maximum values near both walls of microchannel 85

Appendix Figure A.5 (a) Fluorescent microscopic images of anisotropic bacteria absorption at 30 um X 30 um microcubes. Uniform fluorescent intensity at the initial became non-uniform during the bacteria flow was being introduced from the top. (b) Saturation of fluorescent intensity at the site where the bacteria were absorbed. 97

Appendix Figure A.5.1 SEM images of microcubes (50 um X 50 um). The bacteria were selectively absorbed at (a) front/left surface and (b) top/right surface. Inset (i) ~ (iv) showed the magnified image of various surfaces that confirmed the anisotropic absorption 97

Appendix Figure A.6 Microscopic images of bacteria based microrobot movement. It moved in the direction of chemical concentration gradient. The images were captured every 3 seconds and overlaid..... 97

Appendix Figure B Numerically simulated ICP layer for (a) concentration distribution, (b) electrical field and (c) flow field. (d) Schematic illustration for electric potential near the microchamber..... 97

Appendix Figure C Schematic domain of electrochemical membrane system with dielectric pillar array..... 97

Chapter 1. Introduction

1. Perm-selective ion transport

1.1.1 Electrical double layer

Selectivity of the membranes are determined by the surface charge and the pore sizes. Small uncharged particles are more easily to pass through the nanopore compared to the larger ones. The electrical double layer (EDL) is a specific charge distribution at the liquid-solid interface which means that the fixed surface charges on the solid are compensated by mobile counterions in solution [5]. The surface charge at the solid/liquid interface attracts counter ions in the solution to form stern layer and diffuse layer as shown in Figure 1.1. The stern layer is usually described as immobilize thin layer of a few Angstroms thick and the diffuse layer is the mobilized one with free ion movements. The Stern layer and Gouy-Chapman layer together form the electrical double layer (EDL).

The Debye length represent the thickness of the EDL, and is given from Poisson-Boltzmann theory as

$$\lambda_D = \sqrt{\left(\frac{\epsilon_0 \epsilon_r RT}{F^2 \sum_i c_i^\infty z_i^2}\right)}$$

where ϵ_0 is the permittivity of a vacuum, ϵ_r is the dielectric constant of the solution, c_i^∞ is the bulk concentration, F is the Faraday constant, R is the gas constant, T is absolute temperature, z_i is the ionic valence. In general, the Debye

length varies inversely with the bulk ion concentration, which means that high concentration generates a thin Debye length and low concentration generates thick Debye length. The ratio between Debye length and the channel dimension is a critical parameter for permselective ion transportation since it is related to the overlap of EDL.

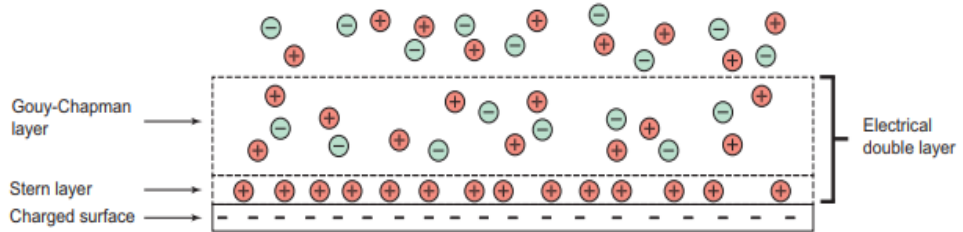


Figure 1.1 The schematic representation of the electrical double layer. The surface is negatively charged. The Stern layer and Gouy-Chapman layer together form the electrical double layer (EDL)

1.1.2 Perm-selectivity in nanochannels

Perm-selectivity refers to the transport of imbalanced ions through the nanostructures. The origin of the perm-selectivity has been claimed to the present day because it is impossible to observe directly in nanostructure itself. However, nowadays, the electrical double layer (EDL) overlap is widely accepted of the main origin of the perm-selectivity. When the pore size of the nanostructure membrane becomes smaller than $O(100)$ nm, the thickness of the Debye layer would be non-negligible and therefore the EDL overlaps the inside of the pore so that the electrostatic repulsion operates the perm-selectivity. Therefore when the nanostructure membrane has negative charge surface, only the positive ions can pass through, while the positive ions cannot due to the electrostatic repulsion. The ratio between the Debye length and the channel dimension is a critical parameter since it is related to the overlap of EDL. Of this unique phenomena observed in nanochannels, the transport of a fluid within a nanochannel, via the application of an external electrical gradient, has many potential applications in the biomedical, energy, and environmental fields.

1.2 Current and potential relationship in an ion-exchange membrane system

Nanofluidics has led to the discoveries of new fundamental findings. One of the findings is the overlapping of an electric double layer (EDL) in nanostructures. The overlapping of EDL allows the permselective transport of ions [6]. Among this related phenomena, Ion concentration polarization (ICP) is considered as one of the unique phenomenon caused by the transport of ions through ion-selective nanostructures. It is one of the fundamental electrochemical transport phenomena that have been observed at nanoporous membranes. Under dc bias, only counter-ions can enter and pass through the charged permselective membrane on the anodic side, while co-ions cannot due to electrostatic repulsion. Therefore, this results to the imbalance of ion concentration on each sides of the membrane. The region with low concentration is called the ion depletion zone and region with high concentration is called ion enrichment zone[1, 2] as shown in Figure 1.2 (a). Due to the depletion of ions as a charging carrier, the conductivity of the ion depleted zone is very small (*i.e.* high electrical resistance). Therefore due to this unique property, the depletion zone itself can be used as a virtual barrier and therefore various applications have been adopted such as purifier and preconcentrator. However, since the current density should be uniform along the microchannel, the magnitude of the electric field is extremely amplified.

inside the depletion zone as shown in Fig 1.2 (b) [7] . Also, inside the depletion zone, various fundamental problems are found such as the electro-osmotic instability[8] and overlimiting current occurs.

Ion concentration polarization (ICP)

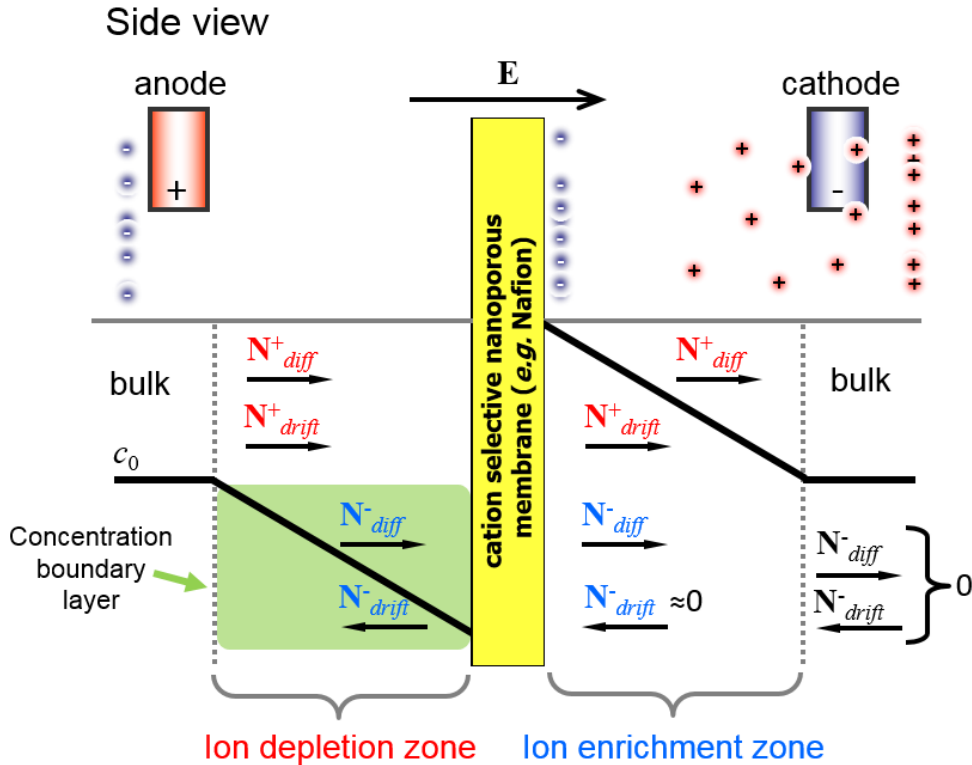


Figure 1.2 (a) Schematic diagram of ion concentration distribution of a cation perm-selective nanostructure which only lets cations pass through. N^+ and N^- are the fluxes of cation and anion, respectively, and the subscripts *diff* and *drift* represent the diffusive and drift ion transport, respectively[9].

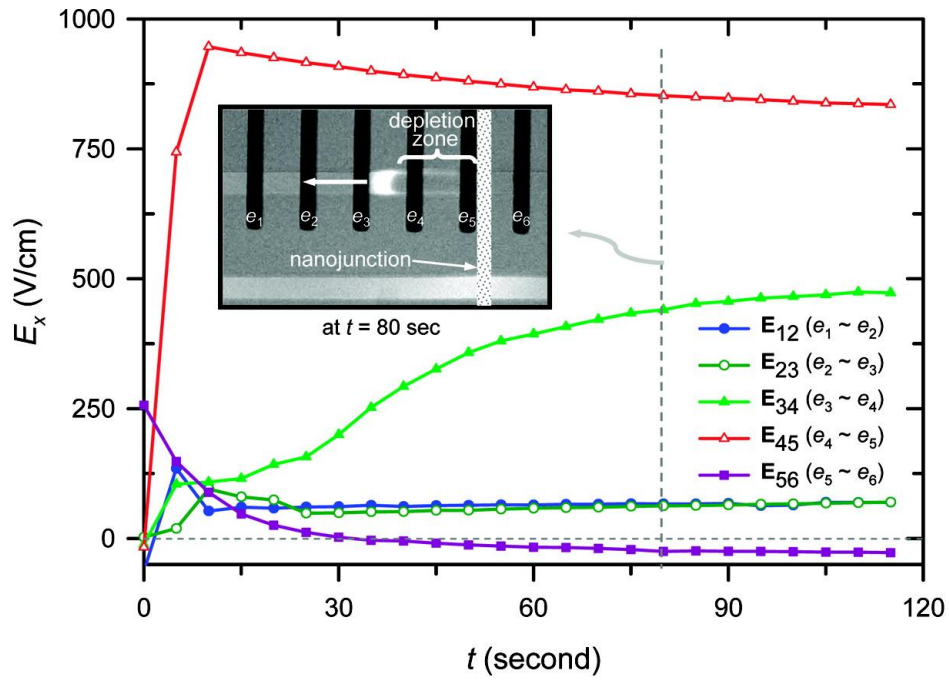


Figure 1.2 (b) In situ measurement of local electric fields inside and outside the ion depletion zone using microelectrodes integrated along the microchannel.

1.3 Current and potential relationship in an ion-exchange membrane system

A typical I–V curve of ion-selective channels includes ohmic, limiting, and overlimiting regimes as shown in Figure 1.3 (a). At first, the I–V curve shows a linear ohmic regime. The current is developing linear with respect to the applied voltage. Linear ion concentration gradient gradually increases and enhances the ion fluxes throughout the ion-selective channels by diffusion. At a critical voltage, the diffusive-flux-enhanced current density saturates when the cation and anion concentrations approach zero, adjacent to the ion-selective channels. Therefore, the limiting current regime is attained and a plateau regime is observed. This behavior can also be explained by the Nernst-Planck equations. The last region the current gets to the overlimiting current(OLC) regime. This regime is an additional ion transportation in the voltage-current characteristics. This can be characterized as a combination of the exponential I-V function to the linearized conductance. OLC has been debated for a period of time, until Rubinstein *et al.*[4] developed a model expressing the OLC shown in Figure 1.3 (b) which was the starting point. Nowadays, most people agree that OLC is mainly attributed to an additional ion transportation by the appearance of the extended space charge layer[4], surface conduction[10, 11], electroconvection[1, 12, 13] and electroosmotic instability [14, 15]

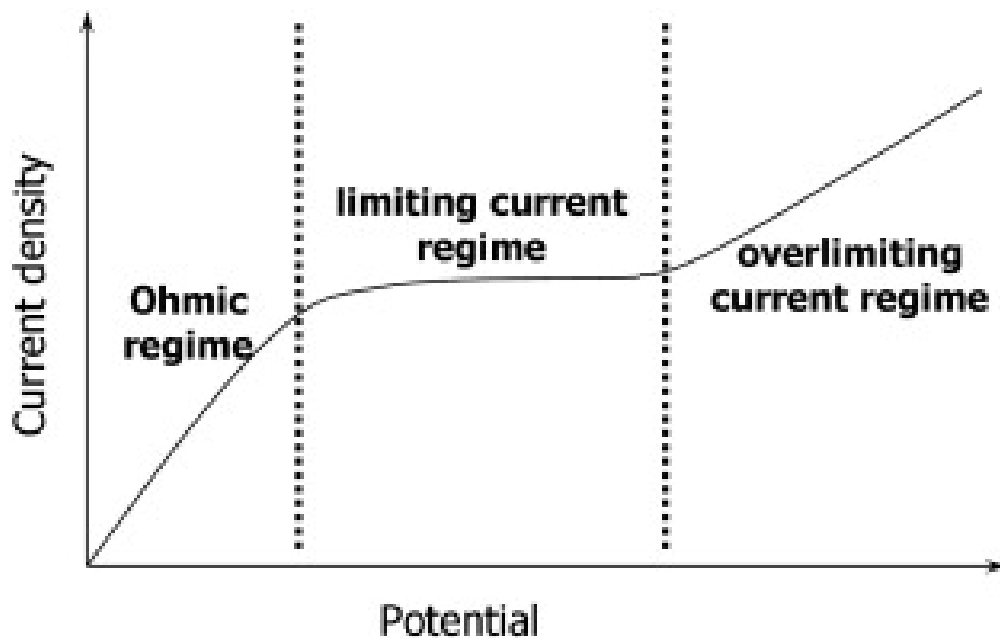


Figure 1.3 (a) The schematic representation of the behavior of a current in a system where there is an electric field applied over a stream of electrolyte is divided by a charge selective interface. The three regions ohmic, limiting and overlimiting can be recognized[16]

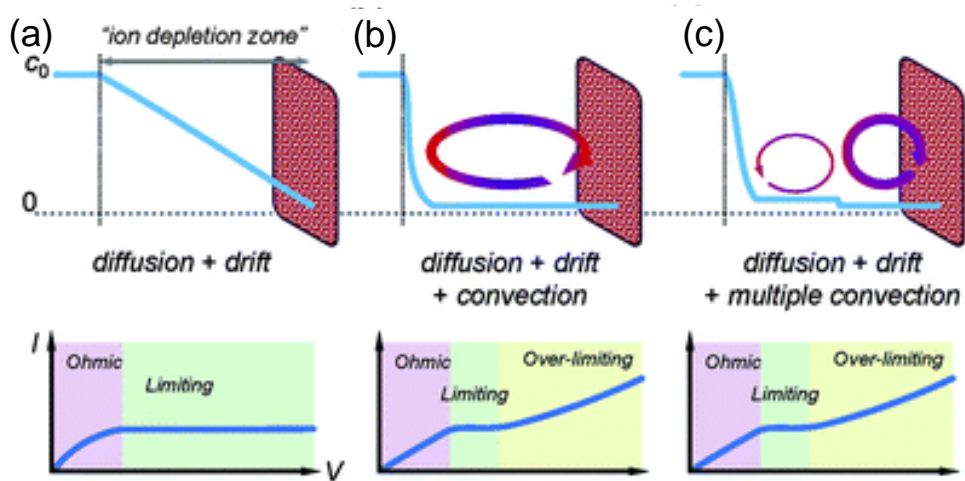


Figure 1.3 (b) The schematic diagrams of the concentration profile inside ICP layer and Ohmic/limiting/over-limiting current behavior when (a) only diffusion and drift were considered, (b) electroconvection was added to (a) and (c) multiple vortices were formed (inducing step-wise discrete concentration distribution).

1.4 Definition terms

Electroosmotic flow (EOF) is a micro/nanofluidic phenomenon in which a movement of the bulk liquid movement of a liquid out of or through a porous material membrane under the influence of an electric field. When the channel is negatively charged, the applied electric field exerts a force on the direction of the cathode on the excess ions of positive charge near the surface.

Ion Concentration Polarization (ICP) is imbalance of ion concentrations at anodic and cathodic side of the nanoporous membrane under dc bias, as only the counter-ions can pass through a selectively charged nanoporous membrane. The regions with low concentration at anodic side is called ion depletion zone and high concentration is called ion enrichment zone, respectively

Surface conduction (SC) is an additional conductivity of an electrolyte in the area of charged surfaces. Close to charged surfaces a layer of counter ions of opposite polarity exists which is attracted by the surface charges.

Overlimiting current (OLC) is an additional ion transportation in the voltage-current characteristics after the plateau regime is observed. This can be characterized as a combination of the exponential I-V function to the linearized conductance. The OLC is mainly attributed to an additional ion transportation by the appearance of the extended space charge layer[4], surface conduction[10, 11], electroconvection[1, 12, 13] and electroosmotic instability [14, 15]

Electroosmotic instability (EOI) is a microscale instability observed during the development of electrokinetic microfluidic applications, and is induced by an interaction between the electric field and fluid motion. The basic mechanism is the effects of field alignment, electroosmotic velocity (convective and absolute instability), channel dimension, periodic forcing, and multiple-species.

1.5 Thesis outline

We experimentally investigated inside and outside of the depletion zone during ICP phenomena by changing the geometry structure of the microchannel and also by installing the pillar structures inside the depletion zone. The geometry effect of the concentration profile, particle tracking, and the electrical responses were investigated. The chapters are divided into 4 chapters. In *Chapter 1*, the background and review of micro/nanofluidic transport will be discussed. *Chapter 2*, we investigated (i.e. the outside of the depletion zone) a multilayer micro/nanofluidic device for selective preconcentration and collection by deforming the microchannel structure and installing pneumatic microvalve system. In *Chapter 3 and 4*, we experimentally investigated the electrokinetic effect[1, 3, 4] (i.e. the inside of the depletion zone) of micro pillars (i.e. spacers in macroscale) inside the depletion zone by multi-physics simulations and micro/nanofluidic experiments. Also, we verified that the physical configuration of a micro pillars (i.e. spacers in macroscale) array has a critical impact for high energy efficient nanoporous membrane platform. In *Appendix A*, experiment was done by employing laminar flow characteristics in attaching *S. typhimurium* flagellated bacteria to the microparticles anistropic ally. *Appendix B and C* are numerical simulations which support Chapter 2 and Chapter 3 individually.

Chapter 2. Selective Preconcentration and Collection of Two Charged Molecules in Microchannels

2.1 Introduction

A number of researches were performed on preconcentration or separation of molecules using conventional high-performance liquid chromatography[17], capillary electrophoresis [18], microfluidic field-amplified sample stacking[19], isoelectric focusing[20], isotachopheresis [21] and temperature gradient focusing [22]. These methods are generally used to produce high purity of therapeutic agents, or to separate chemical reaction products. In practical processes of medical diagnosis systems, these methods have several difficulties. In general, these methods require the additional extraction system of preconcentrated and separated molecules because they employ free flow concept (*i.e.* the operations occur while the samples continuously flow.), limiting subsequent processes. Alternating injection of samples that should be isolated one another causes considerable cross contamination. While the reliability of detection level is enhanced by increasing the concentration of samples, intricate channel geometries or specific chemicals are often demanded for experimental setting. Even after successful separation and preconcentration, online detection processes following the operations can still cause inevitable problems. These problems tend to increase complexity of operations or produce false negative and false positive, resulting in unfeasible on-chip processes. Regulating temperature in microchannels is another critical issue when

temperature dependent processes are needed on chip. Therefore, a new design with simple structure and easy fabrication is demanded for performing fast and accurate separation and preconcentration. Furthermore, a connection to conventional off-chip analysis systems or an integration with on-chip analysis parts is expected for the ideal platform of molecular diagnosis.

As a method to preconcentrate biomolecules, nanoscale electrokinetic phenomenon caused by selective transport of counter-ions in the electrolyte near a nanoporous membrane, called ion concentration polarization (ICP), has been suggested and the preconcentration factor reached up to million-fold [23]. Recently, simultaneous separation and preconcentration, or selective preconcentration, was successfully performed using ICP, demonstrating the separation of phosphorylated and unphosphorylated substrates [24] or tagged and untagged DNA molecules [25]. It indirectly proved that one can utilize the ICP concept not only to preconcentrate low abundant molecules but also to separate molecules with different physicochemical properties. However, these ICP demonstrations still have several limitations. First of all, the preconcentrated sample plug keeps uncontrollably fluctuating due to strong instability of electrokinetic flow inside ICP layer and thus, the identification of the location where reactions occur becomes labor-intensive and time-consuming tasks. Moreover, while the preconcentrated plug pins at a certain location during ICP operation, the background sample is still flowing toward outlets and therefore the collected sample plug at the outlet is inevitably contaminated, diluted or dispersed.

To evolve ICP concept as a practical tool to separate and preconcentrate charged molecules, additional steps of (1) the stable isolation of the highly concentrated sample and (2) on-demand connection to external systems without undesirable dispersion are unprecedentedly required. By designing narrow channels between repeated chambers, the fluidic instability due to amplified electric field inside ICP can be suppressed. Limiting the ever-expanding ICP zone by microstructures [26] or by external hydrodynamic flow injection [27] can improve the hydrodynamic stability and restrict the role of vortices near the membrane. These narrow microchannels between repeated chambers are expected to perform in the same manner. Subsequently, pneumatic microvalve system[28, 29] is employed to isolate the highly concentrated sample from the original sample mixture without further diffusion or dispersion, and also to collect sample plugs so that they can be further used in conventional analytical systems.

In this chapter, we suggest a system that integrates ICP operation and pneumatic microvalve operation. By using pneumatic microvalve system, separated and preconcentrated samples, or selectively preconcentrated samples can be further utilized either on-chip or off-chip.

2.2 Experimental Setup

Figure 2.2 (a) shows the microscopic image of the multilayered selective preconcentration system with pneumatic valve system. We implemented chamber structures repeatedly to suppress fluidic instability and differentiate the flow velocity within a single channel. Buffer channel is connected to the main channel with a perm-selective Nafion membrane. The depth of all microchannel is fixed to 15 μm and three chambers designed by alternating height of 15 μm and 150 μm are located either side from the nanojunction. At the right most chamber, a chamber with the same size is upwardly connected to collect isolated preconcentration plugs. A rib-shaped channel is also subsequently connected to be used as a measurement window. Microvalves (the width and height are 290 μm each) are designed to cover 4 locations as indicated with red ink in Figure 2.2 (a).

For the fabrication, a 4-inch wafer was spun to coat 15 μm layer at 500 rpm of 10 seconds and at 3250 rpm for 30 seconds using SU-8 2015 photoresist (MicroChem. Inc, USA). After 3 minutes of soft bake, the layer was exposed two times to ultraviolet (UV) of 365 nm wavelength for 23.3 seconds (400 mW) using mask aligner. Post bake was for 4 minutes, then was soaked in an isopropyl alcohol (IPA) bath for 3 minutes. For easy detachment of the PDMS device, Trichloro (1,1,2,2-Perfluorooctyl) silane was applied to the master wafer with a vacuum assisted deposition desiccator. PDMS base and curing agent (Sylgard 184 Silicone elastomer kit, Dow Corning, USA) were mixed at 10:1 ratio and desiccated in a vacuum pump for 1 hour to remove air bubbles.

The mixed solution of PDMS and curing agent was poured onto the master and cured in room temperature overnight for the valve layer (Figure 2.2 (b)-(i)), preventing alignment error due to thermal shrinkage.

On the other hand, the mixed solution was poured onto the patterned 4-inch wafer and spun at 1500 rpm for 300 seconds (JSP4A, JD Tech, Korea) to coat 15 μm layer for ICP layer (Figure 2.2 (b)-(ii)). For soft bake, the coated wafer was placed on a hot plate for 30 minutes at 95 $^{\circ}\text{C}$. The PDMS replicas were peeled off from the master and the inlet and outlet holes were punched out. A polymeric nanoporous material, Nafion (20wt% resin, Sigma Aldrich, USA), was used for the nanojunction between the microchannels. A single strip of Nafion (50 μm wide and 1cm high) was patterned on a slide glass using a PDMS piece that has a single straight microchannel and was heated at 95 $^{\circ}\text{C}$ for evaporating solvent after removing the PDMS piece (Figure 2.2 (b)-(iii)). Then, each layer was bonded to a Nafion patterned slide glass by oxygen plasma bonder (Femto Science, Korea) under an alignment through the stereo microscope (SZ61, Olympus, Japan) creating a multilayer. Final assembled micro/nanofluidic device is shown in Figure 2.2 (c).

For sample solution, 0.5 mM KCl solution (Sigma Aldrich, USA) was used with addition of two fluorescent dyes, Sulforhodamine B (SRB) (24.14 nM, Sigma Aldrich, USA) and Alexa Fluor 488 (Alexa) (0.90 nM, Invitrogen, USA). With two different fluorescent colors of orange (SRB) and green (Alexa), their separation and concentration dynamics could be measured and identified.

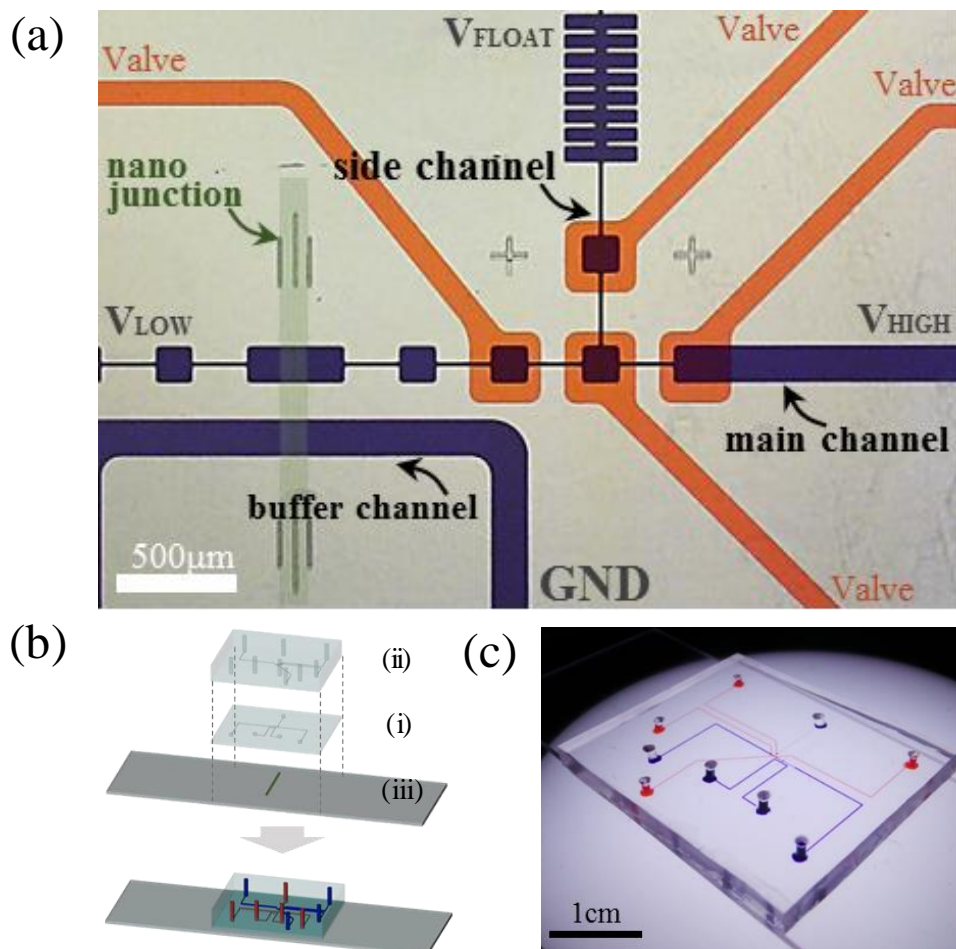


Figure 2.2 (a) Microscopic view of the selective preconcentration device. The microchannels in the ICP layer are indicated with blue ink and the microchannels in the valve layer are indicated red. (b) An exploded view of the device with (i) a valve layer, (ii) an ICP layer and (iii) a Nafion patterned slide glass. (c) Assembled multilayered online selective preconcentration device.

2.3 Device operation

2.3.1 ICP operation

Chemical samples were loaded into the main and buffer microchannel by applying positive pressure from each inlet reservoir. Ag/AgCl electrodes were inserted into the inlet and buffer reservoirs on the device and connected to a power supply (Keithley 6517, Keithley Instruments, USA and Keithley 238, Keithley Instruments, USA). For applying the electric field, voltage control was required on each of the four reservoirs. For the continuation on separation and preconcentration, 90 V and 60 V were applied to the reservoir of the main channel while the reservoir of the buffer channel was grounded. The motion of fluorescent dyes were tracked by inverted fluorescence microscope (IX53, Olympus, Japan) and recorded by CellSens (Olympus, Japan) computer program.

2.3.2 Pneumatic microvalve operation

A compressor (Gfrog, Stylex, Korea) as a pressure source was connected to several mini solenoid valves (SY 3120, SMC pneumatic, Korea) and a polystyrene tube connected a solenoid valve and an inlet of valve layer in a PDMS device. Before the connection, DI water was filled into the microchannels of valve layer to reject air bubbles into the ICP layer. In order to manipulate the pneumatic microvalves automatically, a customized LabVIEW code (National Instrument, USA) and a DAQ board (USB-DAQ 6341, National Instrument, USA) were used.

The valve operation consisted 3 steps as shown in Figure 2.3.2. Step1 (ICP preconcentration): Valve 1 was closed when selective preconcentration was in process. Step2 (Isolation): When the targeted preconcentration plug reached the chamber which was connect to the side channel, valve 1 was open and valve 2 and 4 were closed to isolate the sample plug from the main channel. Step3 (Collection): Then, by closing valve 1 and 3 while valve 2 and 4 still were closed, the isolated plug was squeezed into the measurement window. Fluorescent dyes diffused into a larger area and the fluorescence intensity was analyzed without being saturated. By leaving valve 1 closed and others open, the whole 3-step process could be repeated for further collections. One can control the duration of Step1 to obtain a different amplification ratio.

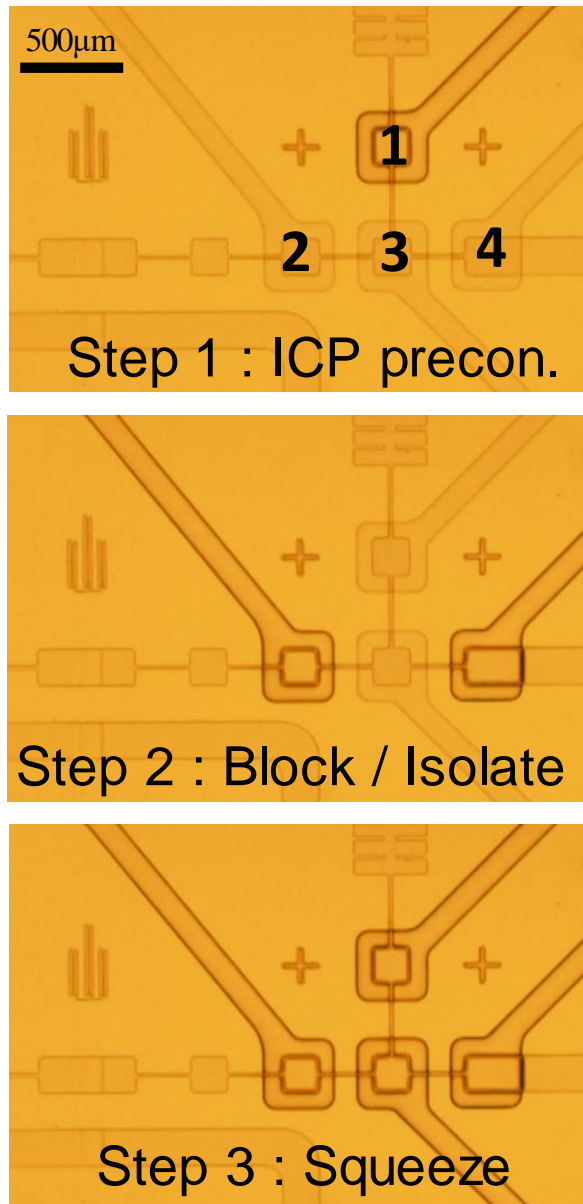


Figure 2.3.2 Microscopic images of 3-step valve control sequence: Step1 – ICP preconcentration to form a high concentration plug, Step2 – isolation of a highly preconcentrated plug at specific chamber, and Step3 – collection of the highly preconcentrated plug into upward channel.

2.4. Results and discussion

2.4.1 Selective preconcentration

Figure 2.4.1 (a) demonstrates that two different dyes were simultaneously preconcentrated and separated over time. Without electric field along the nanojunction, no fluorescent dyes were observed in the channel because the initial concentrations of dyes were too low to be detected. As we applied 90 V for V_{HIGH} and 60 V for V_{LOW} on each end of the main channel with grounded buffer channel, ICP was triggered near the membrane. Since the nanoporous membrane was cation-selective, only cations could pass through the membrane, creating ion depletion zone with no charged species for charge balance at the anodic side of the membrane. As reported in previous researches [30], it caused significant and dynamic perturbation in local ion concentration and in amplified electric field near the membrane along with the generation of strong electrokinetic flow. The high electric field gradient at the boundary of depletion zone rejected the penetration of charged molecules into the ion depletion zone so that both dyes stacked and detected at the boundary.

At the beginning of selective preconcentration, both dyes were preconcentrated in the chamber 1. After the ion depletion zone became stabilized over time, the preconcentrated plugs of two dyes with different mobility were separated. This separation was drawn by the equilibrium between electroosmotic drag force and electrophoretic force as described in Figure 2.4.1 (b) [24]. The electroosmotic drag exerted on the molecules was $\mathbf{F}_{\text{drag}} = 6\pi\mu R\mathbf{u}$ when μ is the dynamic viscosity, R is the radius of the spherical object, and \mathbf{u} is

the electroosmotic velocity of bulk which is independent from molecule's properties, while the electrophoretic force exerted on the charged species was $\mathbf{F}_{EP} = q\mathbf{E}$ where q is net electric charge and \mathbf{E} is electric field. According to an experimental observation shown in Fig.2 (A), Alexa (green) moved toward the V_{HIGH} while SRB (orange) stayed near the depletion zone boundary. Since \mathbf{F}_{drag} is mainly determined by R which is almost the same value for SRB and Alexa, the value of net charge plays a key role in determining the equilibrium positions balanced by \mathbf{F}_{drag} and \mathbf{F}_{EP} . This argument is in line with the experimental result since the net charge of SRB and Alexa is -1 and -2, respectively.

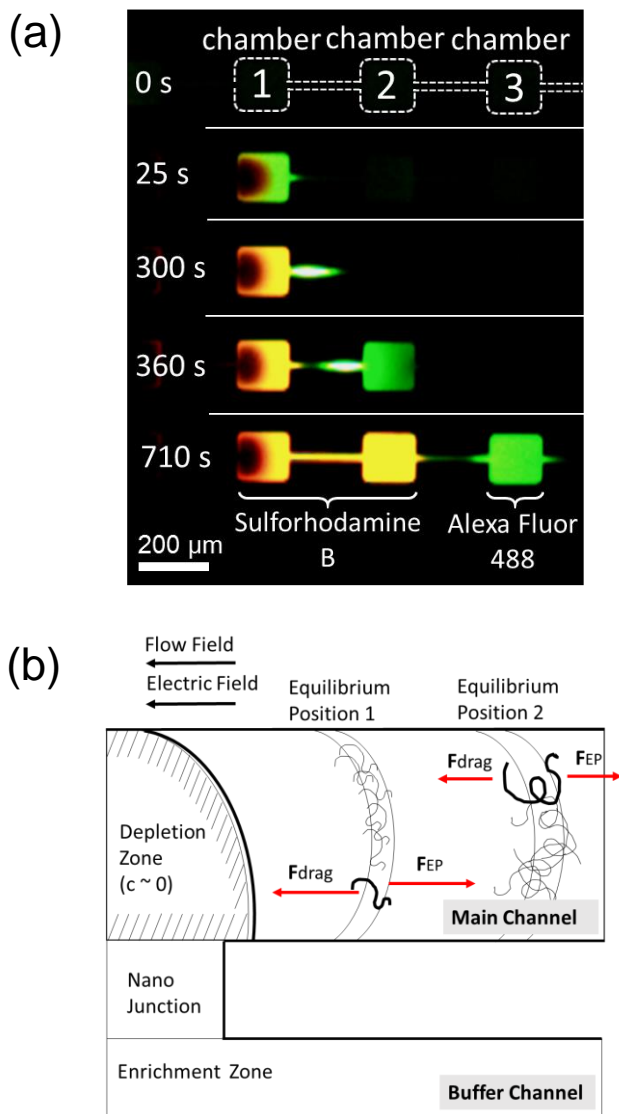


Figure 2.4.1 (a) Time-lapse images of selective preconcentration of SRB and Alexa. High concentration ratio is represented by the brightness of fluorescence. Since the physicochemical properties of two dyes were different, they were preconcentrated at different locations. (b) Schematic diagram of selective preconcentration mechanism with different mobility. The separation was drawn by the equilibrium between electroosmotic drag force and electrophoretic force exerted on molecules.

2.4.2 Stabilization of selective preconcentration

While the phenomenon of different equilibrium positions of molecules with different mobility has been already reported in previous researches [31], due to the strong instability by local amplified electric field near the nanojunction [30], one strong plug and one smaller plug in parabolic shape were reported and the locations of preconcentrated plugs were always unpredictable instead of stably generated plugs with high concentration. Therefore, it is important to control the positions of the concentrated sample plugs and to stabilize the ion depletion zone. In our system, the repeated narrow and wide channels stabilized the depletion zone by the geometry restricting the expansion of vortices and strong electrokinetic flows in ion depletion zone, thereby forming well-defined plug profile. Consequently the control of each accumulated molecules' location became simple and tailing effect was reduced. This alternating geometry also differentiated the velocity of the fluidic flow at the boundary between the narrow and the wide channel, and therefore, it increased the efficiency of separation and helped the membrane microvalve system for further blocking and squeezing of the molecules.

2.4.3 Quantitative analysis for separation and preconcentration efficiency

The selective preconcentration was quantitatively analyzed by measuring pixel intensity with fixed exposure time. The intensity of the original sample and reference solutions at different concentrations were compared to accurately compare the preconcentration ratio, since the pixel intensity is not linearly proportional to the concentration of dyes. As shown in Figure 2.4.3 (a), the average pixel intensity of dyes increased in each chamber in order. The both dyes (Alexa + SRB) were rapidly preconcentrated in the chamber 1 from the initial to 10 minutes. From 10 minutes to 25 minutes, the green plug (Alexa) moved to the chamber 2 while the intensity of the plugs simultaneously increased. This agrees with the microscopic image in Figure 2.4.1 (a) that the orange plug (SRB) stayed in the chamber 1 while the green plug (Alexa) moved to the chamber 2. After 25 min, the green plug (Alexa) moved to the chamber 3 while the average pixel intensity of the chamber 2 sharply diminished. In this point, the average pixel intensity of the chamber 2 did not decrease to zero. This is because the orange plug (SRB) was saturated in the first chamber so that it went on to the chamber 2. In the chamber 3, the average pixel intensity reached up to 98.2, which means that the green plug (Alexa) was preconcentrated above 100-fold since the average pixel intensity of 10X, 50X, and 100X concentrations on Alexa Fluor 488 was 12.9, 58.9, and 95.3 respectively. After 30 minutes, the repeated microvalves operation were started, showing severe fluctuations and this part will be discussed later.

In previous researches, the two separated plugs have been distinguished only

by their positions since only one dye was tagged for two or more different kinds of molecules [24, 31]. Compared to these works, RGB color profile was rigorously investigated to validate the separation of two molecules. Since the emission from SRB has both red and green color, it is efficient to measure color intensities from chamber 3 as an indicator of separation, where only Alexa dye was preconcentrated. Since the pixel intensities of blue and red were almost the same, only red and green colors were discussed. The color profile of 100-fold reference solution of Alexa with 0.90 nM was 33.28 in red and 219.76 in green under the exposure time of 300 ms. As shown in Figure 2.4.3 (b), the pixel intensity of the chamber 3 in the main channel was 223.20 in green and 31.17 in red at the operation time from 25 minutes to 30 minutes, which agreed with the reference values of the 100-fold, meaning that the majority occupying the chamber 3 was only Alexa dye. In addition to this, the color profile of the chamber 1 (Figure 2.4.3 (c)) contained high value of red color which was not found in the chamber 3 as shown in Figure 2.4.3 (b). The ratio of red and green color was reversed at 10 minutes and maintained around 2:1 from 25 minutes to 30 minutes in the chamber 1. Since SRB was dominant in the original solution (SRB at 24.14 nM + Alexa at 0.90 nM) and its red/green ratio was 2:1, we can conclude that the chamber 1 was solely occupied by SRB after 25 minutes. This color profile measurement can provide an accurate platform to measure the separation efficiency between two dyes with different mobility.

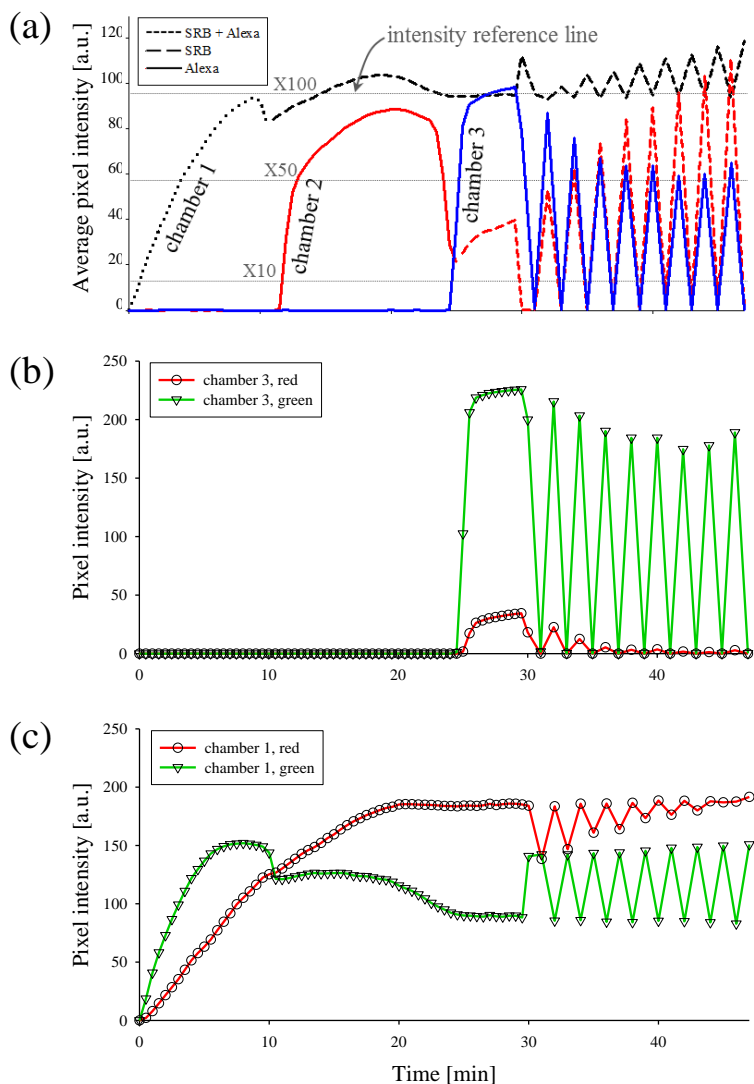


Figure 2.4.3 (a) Overall fluorescence intensity tracked in each chamber as a function of time. The concentration ratio of selectively preconcentrated Alexa in chamber 3 exceeded 100-fold, maintaining the preconcentration factor high enough in repeated valve operations. (b) Red/green color profile in chamber 3, showing the chamber 3 only has Alexa. (c) Red/green color profile in chamber 1, showing the chamber 1 only has SRB. Fluctuations after 30 minutes in all plots are due to microvalve operations.

2.4.4 Isolation of preconcentrated plugs by valve system

As the operation continued further, the preconcentration factor increased accordingly. However, subsequent process using selectively preconcentrated molecules was difficult since the selective preconcentration was performed while the background solution freely flows in a single channel. Besides, subsequent on-chip process which should exclude electrical operation is inapplicable because the plug drastically dispersed as shown in Figure 2.4.4 (a) when the applied voltage was turned off. To resolve this problem, a method is required in which the plug is isolated and transported to another site, while the amplification ratio maintains without loss for either on-chip or off-chip applications. This can be realized by using pneumatic microvalve system. To guarantee the role of valves to block the plug from the original sample channel, the extent of diffusion was compared between the case of valve OFF and valve ON as described in Figure 2.4.4 (a) and Figure 2.4.4 (b).

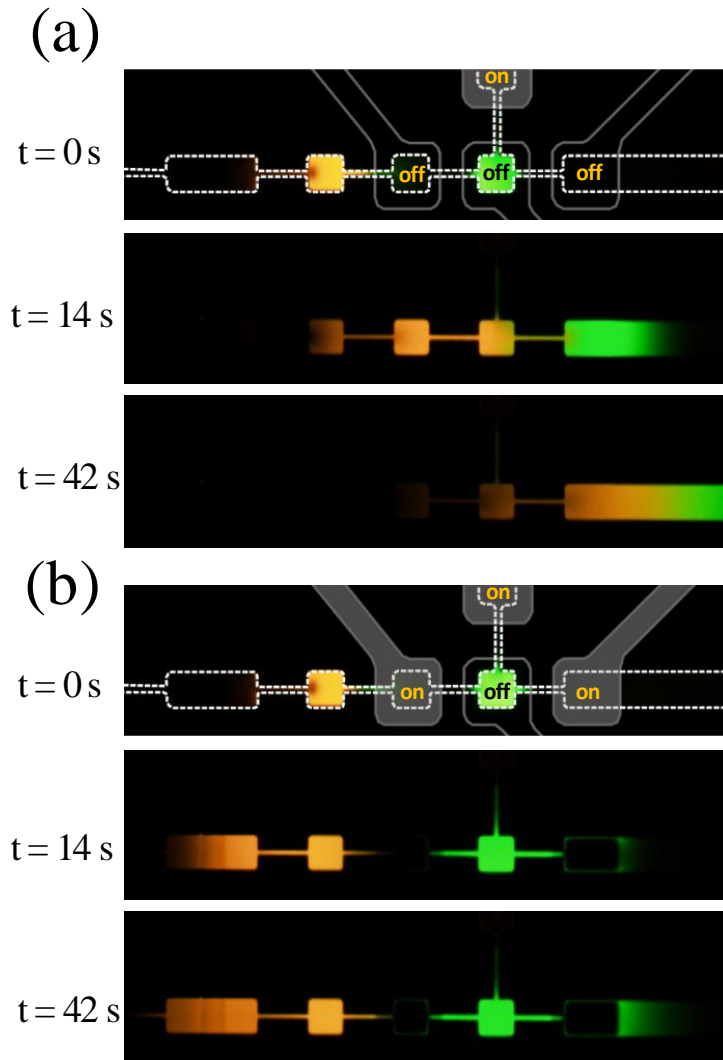


Figure 2.4.4 Time-lapse images showing the dispersion of isolated plug when the valves are (A) OFF and (B) ON.

2.4.5 Collection of pre-concentrated plugs by valve system

The valves were operated in a repeated cycle as described in Figure 2.3.2 (d) to collect the selectively pre-concentrated plug into the side channel. In a cycle, the plug was isolated from the original sample solution and squeezed up. To analyze the pre-concentration factor achieved from the process, a rib-shaped measurement window was installed in the middle of the side channel. This measurement window was designed for metering how high the concentration rate will be achieved through the process. In the meantime, the measurement window has larger area compared to the side channel itself so that it has low fluidic resistance, allowing subsequent processes without any disturbance. Moreover, the windows showed diffusion effect laterally when pre-concentrated plugs were moved up into the side channel. As shown in Figure 2.4.5 (a), no fluorescence intensity was observed in the measurement window at the initial. By the first valve operation, the pixel intensity of measurement window already exceeded 10-fold of the initial concentration of Alexa as plotted in Figure 2.4.5 (b). With repeated valve operations, the concentration of collected plugs in the measurement window continuously increased so that the concentration reached over 30 times of the initial concentration after sixth operation. After ninth collection, it was observed that the measurement window was fully filled with green dyes.

The pre-concentration factors of each Step1 in repeated cycles were maintained high enough to continuously increase the pixel intensity of the measurement window. Figure 2.4.3 (a) also supported this result. In the figure,

the valves were repeatedly operated in the same cycle with the interval of 2 minutes after 30 minutes of whole operations. When the molecules selectively preconcentrated in the chamber 3 were isolated by valves and moved up into the side channel, the pixel intensity of the chamber 3 decreased whereas it increased again while the molecules were selectively preconcentrated again in a next cycle for 2 minutes. During 9 times of valve operations, the concentration of preconcentrated molecules in the chamber 3 was maintained over 50-fold compared with a reference value. The upheld high amplification ratio of collected sample was led by stable and reproducible valve operations. Since microvalve systems squeezed preconcentrated plugs by mechanical force, the mechanism of the collection process was barely agitated while electric field was applied through the channels, allowing repeated implementation of valve operations.

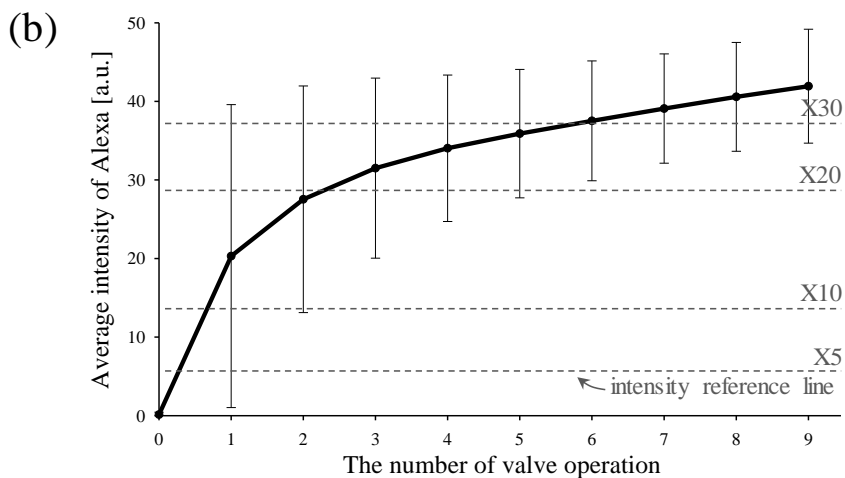
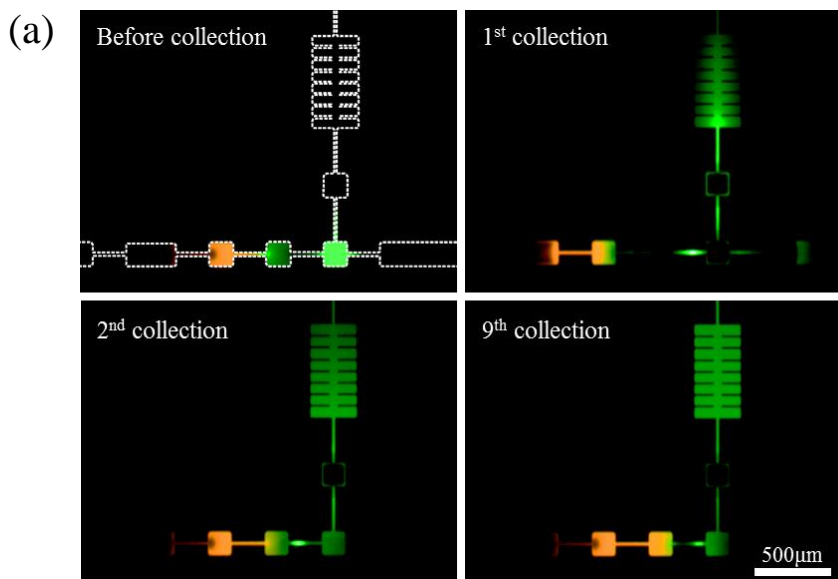


Figure 2.4.5 (a) Snapshots of repeated valve operations collecting selectively preconcentrated plugs. Compared to the initial state, the measurement window was being filled with green dye (Alexa) over several valve operations. (b) Average intensity change in the measurement window over number of repetition of valve operations. The average intensity exceeded 10-fold in a single valve operation, and 30-fold after nine operations. Note that there was no SRB in the measurement window.

2.5 Conclusions

In this work, we demonstrated a multilayer micro/nanofluidic device for selective preconcentration. The operating principle of the device is based on the high electric field gradient induced by ICP phenomenon. In the main channel, two opposing electrophoretic force and electroosmotic drag force acting on the charged molecules are balanced depending on the physicochemical properties of the molecules. The molecules were accumulated up to 100-fold at different equilibrium positions. By introducing pneumatic microvalves, diffusion and dispersion due to the high concentration gradient were prevented. Also by sequentially operating the microvalves, highly concentrated samples could be separated from the main channel without losing their high amplification ratio. Given the importance of preconcentration/separation in molecules, we expect that this mechanism and structure of the micro/nanofluidic device would be a powerful tool for diagnostics, biology researches, and point of care systems.

Chapter 3. Surface Conduction and Electroosmotic Flow Contribution on Perm-Selective Ion Transport

3.1 Introduction

Perm-selective ion transportation through nanoporous membrane have gained a great attention for fundamental electrokinetics studies and developing its innovative engineering applications. Traditional electrodialysis (ED)[32-35] systems is one of the representative platforms where the perm-selective ion transport leads a distinguishable overlimiting conductance (OLC)[36] due to concentration polarization phenomenon and the efficient salt removal for desalination capability[37-40]. The working principle of ED is that source water injected into a serial stacking of cation-exchange- and anion-exchange-membrane was separated into waste water and fresh water with perpendicular electric field across the membranes[41, 42]. Thus, spacers inside this ED system should be installed between the membranes to prevent any physical- and electrical- contact. However, it was reported that the dielectric spacers have a negative impact on the ion transport due to the current shadow effect[43] although they provides enhancement mechanism of mass transfer *via* mixing promoters [41] or local flow redistribution [44]. The spacers lead to high electrical resistance of the whole system (*i.e.* lower OLC and worse power consumption) because the ions itself do not migrate where the spacers are located. While a conductive spacer[45-47] has been utilized as a conduction

promoter[41, 48, 49], it is difficult to manufacture the conductive spacers and it can easily lose conductivity due to physical breakdown by changing the structure.

Instead, in this work, we suggested avoiding the current shadow effect of the spacer by reducing length scale of such system, while the dielectric spacer was kept being used. It has been reported that the length scale is a critical parameter to distinguish the driving mechanism of perm-selective ion transportation[10, 11, 50]. Depending on the characteristic length scale, the driving mechanism is categorized into (i) surface conduction (SC)[36, 51, 52], (ii) electroosmotic flow (EOF)[1, 13, 53, 54] and (iii) electro-osmotic instability (EOI)[2, 14, 55-57]. The length scale of typical ED system lies in EOI regime[58] so that reducing convection by spacer would lower the ion transport. However, a microfluidic confinement would enhance the ion transportation since the length scale of such system is typically within the SC or EOF dominant environment [36, 52, 59, 60]. As expected, preliminary measurement with or without micro dielectric pillar structure (which mimicked the spacer in ED system) can enhance OLC as shown in Figure 3.1 (a). In such confinement, the electrical double layer (EDL) [61-64] around the dielectric pillar with negatively charged surface contributes to additional ion transport through SC and EOF mechanisms as shown in Figure 3.1 (b). SC and EOF promotes the ion transportation by direct conduction within EDL and by initiating additional flow begun from EDL, respectively.

In this study, we rigorously investigated the electrokinetic effect[1, 3, 4] of the micro dielectric pillar in a micro confinement environment by multi-physics simulation and micro/nanofluidic experiments. Both numerical simulations and *in situ* visualizations confirmed the additional ionic current by SC and EOF. Individual roles of SC and EOF are extracted and compared with various electrokinetic parameters such as EDL thickness[65, 66], surface charge of dielectric pillar and external electric field. Furthermore, we presented the effects of physical configuration of dielectric pillar array on OLC, which was not a typically considered in previous studies. Thus, the conclusion extracted from this analysis would provide general strategy for designing highly energy-efficient electrochemical membrane platform.

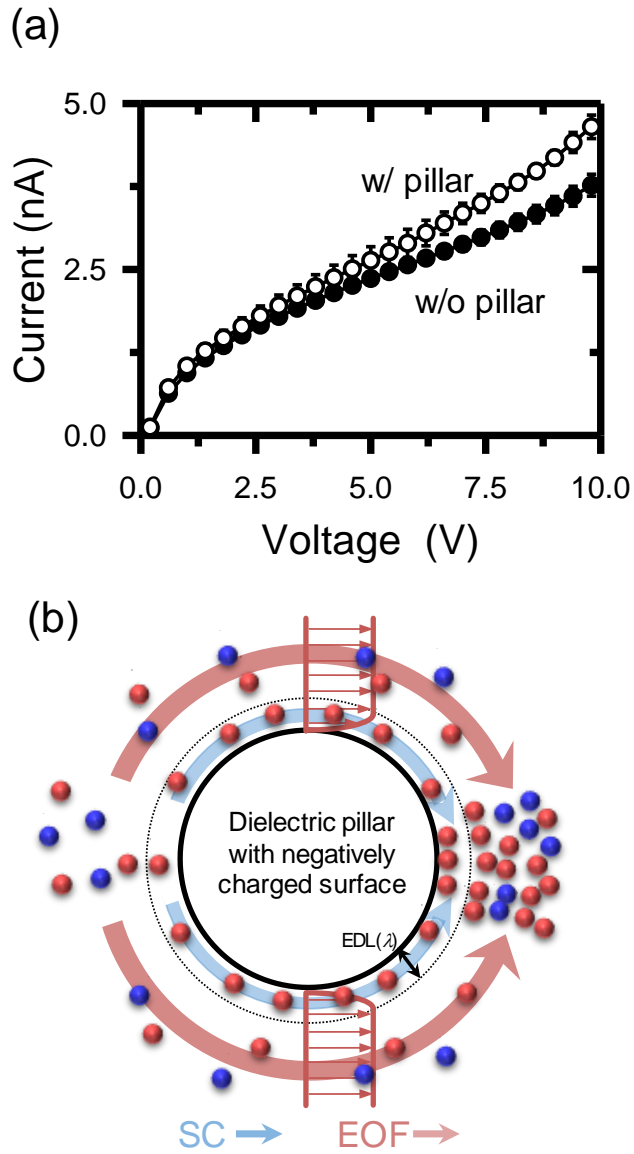


Figure 3.1 (a) Preliminary experimental current-voltage characteristics of micro/nanofluidic device with and without micropillar. (b) Schematic diagram of two mechanisms of perm-selective ion transportation; (i) surface-driven electroosmosis and (ii) surface conduction through electrical double layer on the dielectric pillar.

3.2 Experimental setups

To investigate the effect of the dielectric pillar, the design of the microchannel is shown as in Figure 3.2 (a) and (b). The pillar array (15 μm radius and inter-pillar distance of 95 μm and 100 μm) were installed inside the main microchannel. We examined two types of pillar configuration; staggered type and aligned type. On the main microchannel, we added side microchannels on both sides of the main- and buffer-microchannel for the easiness of the experiment [4]. The dimensions of the microchannel were as following; the main- and buffer-microchannel: 200 μm width \times 15 μm depth \times 6mm length; the air valve microchannel: 15 μm width \times 15 μm depth. General PDMS fabrication steps were used to fabricate the device [5]. The Nafion nanoporous membrane was patterned on the glass substrate based on surface patterning method [6]. Simply, Nafion was patterned using a straight microchannel (200 μm width \times 50 μm depth) on a glass side, and the PDMS piece of main microchannel was irreversibly bonded by plasma bonder (CuteMP, Femto Science, Korea) to a designated position on top of the Nafion-patterned glass.

Chemical preparation. For visualization of the experiments, two mixture of solutions were used; (i) A mixture of KCL solution (Sigma-Aldrich, USA) at a concentration of 0.1mM with charged fluorescent dye Alexa Flour 488 (1 μM , Invitrogen, USA) for the observation of the concentration profile and (ii) the same mixture with canola-oil droplets for tracking the flow field. Canola-oil was ultra-sonicated for 6 minutes for forming micro-oil droplets (average

diameter = $\sim 2 \mu\text{m}$). Canola oil is neutral, but become charged droplet when it break below few micrometer scale. Note that typical tracer such as polystyrene microparticle has high surface charge so that they are mostly rejected from the entrance of IDZ.

Experimental setup. In the microfluidic experiment, the concentration profile inside the ICP layer and the tracers near the pillar array were imaged by an inverted fluorescent microscope (IX53, Olympus) and the CellSens program. Using Ag/AgCl electrodes, external electric field was applied by a source measure unit (Keithley 236, USA). Current-voltage response were cyclically measured in the range from 0 V to 10 V ($0\text{V} \rightarrow 10\text{V} \rightarrow 0\text{V}$) at $\pm 0.2 \text{ V}/30 \text{ sec}$. The current values were automatically recorded at every step by customized LabView program.

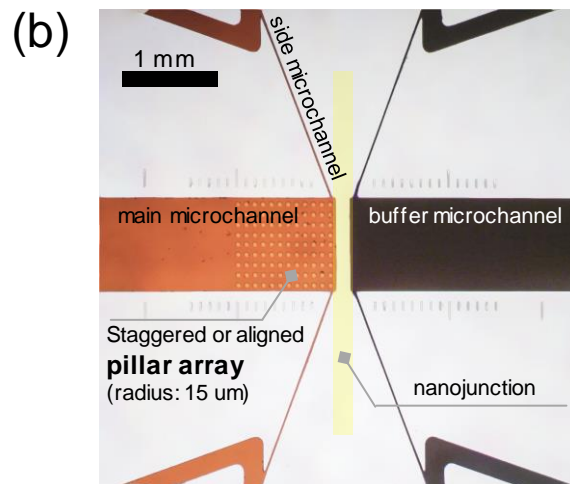
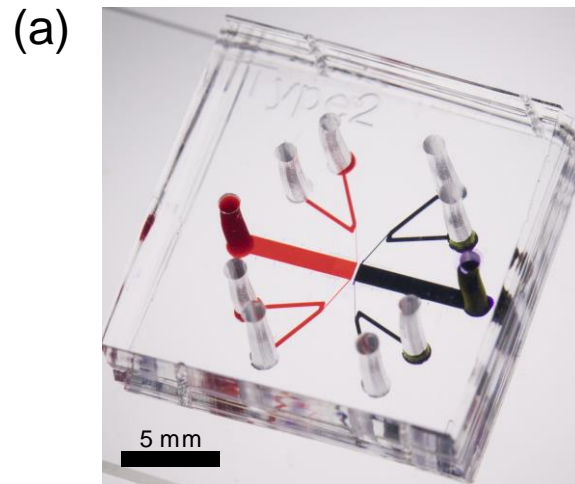


Figure 3.2 (a) Snapshot and (b) microscopic images of fabricated micro/nanofluidic device, integrated with the dielectric pillars on anodic side.

3.3 Results and discussion

3.3.1 Dielectric pillars inside the ion depletion zone

In order to investigate the effect of dielectric pillars inside IDZ, one should determine the number of pillars in the device shown in Figure 3.3.1. Electric potential was applied to the main microchannel and the buffer microchannel was grounded so that IDZ is formed at the main microchannel where the pillars were installed.

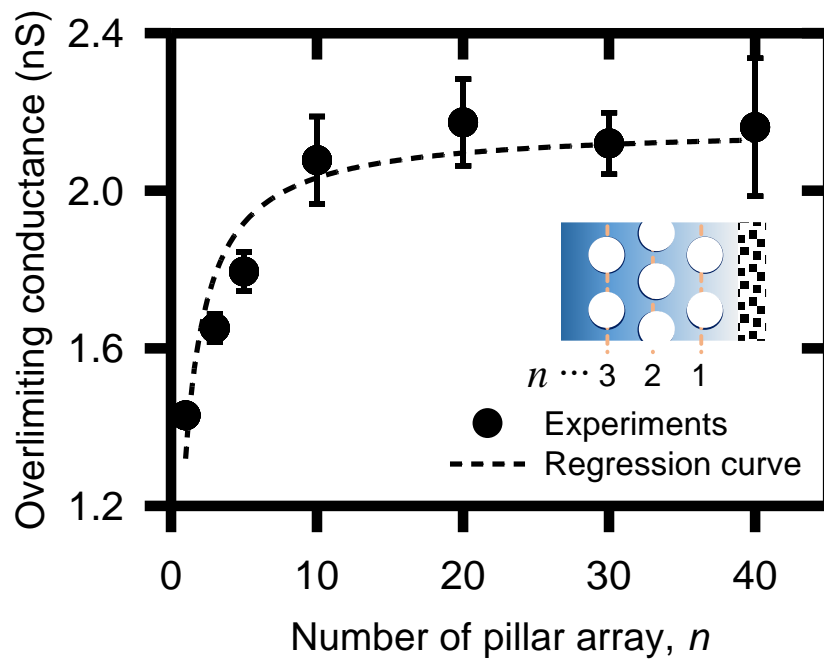


Figure 3.3.1 Experimentally measured OLC depending on the number of pillar array.

3.3.2 Electrokinetic effects of charged dielectric pillar at SC and EOF regime

While EOF plays a dominant role for the perm-selective ion transportation in macroscale system such as ED, SC or EOF lead the transportation in micro-confined environment shown in this work. SC caused by the EDL of the dielectric pillar results an additional local ICP around each pillar as shown in Figure 3.1 (b). Additional ion depletion zone (AIDZ), which decreases the electrical conductance, forms at the back of each pillar (i.e. the location facing the bulk) and additional ion enrichment zone (AIEZ) which increases the electrical conductance appears at the front of each pillar (i.e. the location facing the cation-selective surface). Since the dielectric pillars were arranged under appropriate separation distance, a number of AIEZ formed inside IDZ can create additional current path, while the current barely flows through IDZ in the case of non-pillar microchannel. Thus, the AIEZ resulting from SC increases the electrochemical efficiency of the system by directly serving the abundant charge-carrier toward the nanoporous membrane. EOF is the motion of fluid only in a microchannel or a microcapillary under an external electric field. Thus, EOF should appear around each dielectric pillar to enhance the ion transportation to the AIEZ. Due to the combined contribution of SC and EOF caused by the dielectric pillars enhances the additional ion current transport by forming multiple AIEZs.

The dominance of SC and EOF are reported to be varied with (i)

surface charge of substrate and (ii) Debye length around the dielectric pillar (i.e. bulk concentration) [20]. Pillars with thick Debye length and high surface charge drive the system to a SC-dominant regime and pillars with thin Debye length and low surface charges contribute the system to be EOF-dominant regime. When the surface charge converges to zero, the electrokinetic effect of the dielectric pillar is vanished, which has been the research subject of the non-conductive spacer in the ED system [12]. Therefore, confirming the formation of AIEZ at the front of dielectric pillars and electroosmotic flow around the dielectric pillars would be a key evidence of SC- and EOF-dominant regimes in the case of micro/nanofluidic device. In this study, the effect of aforementioned parameters (i.e. surface charge and Debye length) on SC and EOF will be presented and also the alignment type of dielectric pillar array will be investigated as well.

3.3.3 SC and EOF in staggered dielectric pillar configuration

As shown in Figure 3.3.1, OLC increased and saturated as a function of the number of dielectric pillar array. This was attributed to the AIEZ and electroosmotic flow can enhance OLC, but the dielectric pillars outside IDZ would merely affect to OLC. Thus, we set the number of dielectric pillar array to let the IDZ remain inside the dielectric pillar arrays.

The first configuration is a structure in which a pillar with a radius of $15\ \mu\text{m}$ is arranged in a staggered pattern. The simulation and experimental result of concentration profile inside IDZ are shown in Figure 3.3.3 (a) and Figure 3.3.3 (b), respectively. Note that only SC and EOF were considered in the simulation. As a result, it can be clearly seen the AIEZ in the front of each pillar, especially the first column from the membrane (Figure 3.3.3 (a)). Thus, concentration gradient inside IDZ in this configuration is largely deformed due to SC and EOF. While the deformed concentration gradient was observed in the experiment as well, AIEZ or AIDZ are weakly observed (Figure 3.3.3 (b)). Because the formation of AIEZ is occurred due to EOF as well, the simulated flow field and experiment tracking were shown in Figure 3.3.3 (c) and 3.3.3 (d), respectively. As expected, a strong and localized vortex was formed counterclockwise at the top and clockwise at the bottom of each pillar to satisfy the continuity condition. Since EOF is surface driven flow, the speed of vortex is non-uniform (faster in the vicinity and slower between pillars). This was clearly observed in the flow field tracking experiment (Figure 3.3.3 (d)). Micro oil droplet inside IDZ initially

pushed back toward the reservoir along with the expansion of IDZ. Momentarily, the droplet started to be trapped as vortex at high speed near the pillar and low speed in the bulk. Note that not every dielectric pillar was able to capture the tracer because most of tracer escaped from IDZ even oil has low surface charge. As shown in these flow field tracking, each vortex rotated locally so that EOF contributed to the ion transport only for individual pillar.

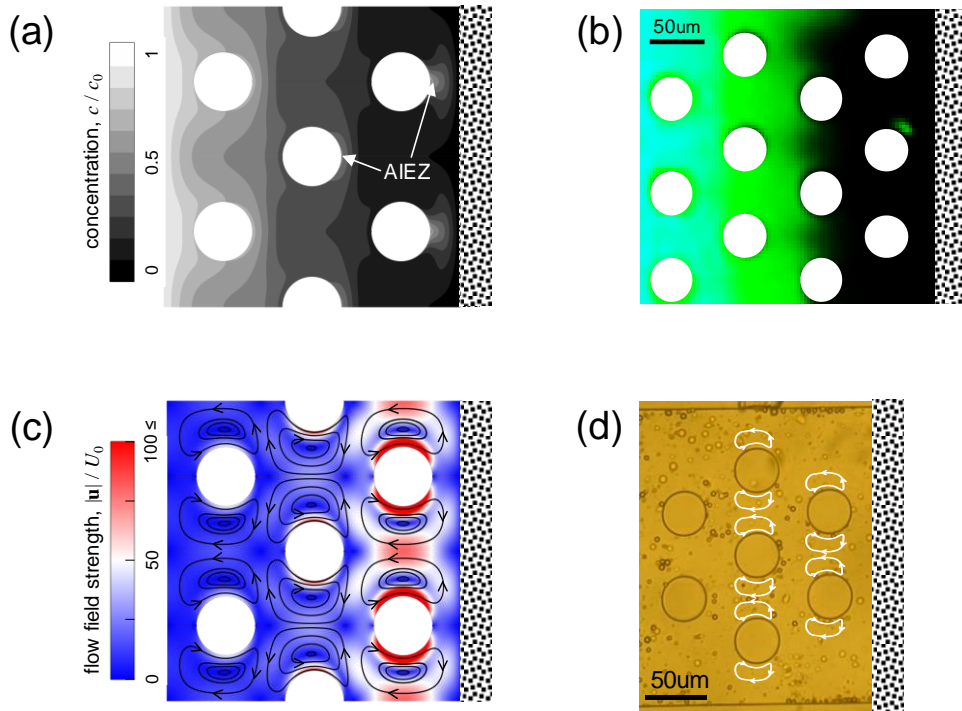


Figure 3.3.3 (a) Numerically simulated and (b) experimental visualized deformed concentration profile of the staggered dielectric pillar configuration. The numerically obtained concentration profile is normalized by bulk concentration c_0 . (c) and (d) are the flow field simulation and flow tracking experimental results of the staggered configuration, respectively.

3.3.4 Current-voltage characteristics depending on surface charge density and Debye length of the staggered configuration

SC and EOF almost equally contribute the current throughput (or current density) depending on electrokinetic parameters. To divide each contribution, a numerical simulation is conducted as shown in Figure 3.3.4. Each plot represents the EOF only- (red dash dot line) and SC only- (blue dash line) contribution and overall current density (black solid line) as a function of applied voltage. The tile of plots is generated as a function of surface charge density for column and Debye length for row. Note that bottom most plot of the third column is the case of ineffective condition (*i.e.* the current density stays at its steady value). Among the plots, the practical experimental conditions in this work are closed to the second column (blue backgrounded plots) demonstrating the nearly equal contribution of SC and EOF. Lowering surface charge density and decreasing Debye length would enhance the EOF contribution (*i.e.* toward the bottom plot of the first column) and *vice versa* for the SC contribution. Nonetheless, SC and EOF are almost equally contributed as compared to the aligned configuration which will be demonstrated in the next section.

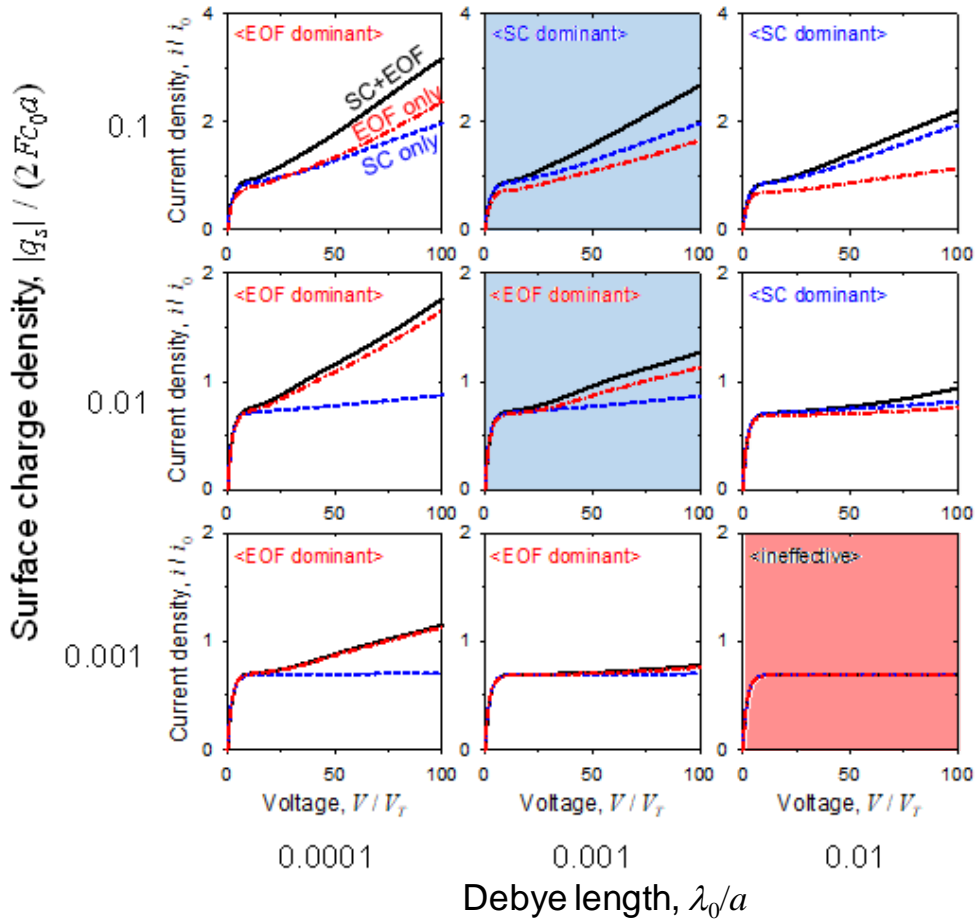


Figure 3.3.4 Current-voltage characteristics depending on surface charge density and Debye length of the staggered configuration. In these tile plots, q_s is the surface charge density of dielectric spacer, F is the Faraday constant, a is the radius of the dielectric spacer and λ_D is the Debye length. The denoted surface charge density and the Debye length are dimensionless. In each plot, current density and applied voltage are normalized by limiting current scale $i_0 = 2FDc_0 / L$ and thermal voltage scale, respectively.

3.3.5 SC and EOF in Aligned dielectric pillar configuration

The second pillar type is an aligned configuration. As demonstrated in previous section, the computed and visualized concentration profiles are shown in Figure 3.3.5 (a) and 3.3.5 (b), respectively. In this configuration, the concentration gradient in IDZ is more deformed than the staggered configuration. While IDZ still exist between each row of pillars, AIEZs are connected along each row of pillars. Thus, more charge-carriers in a stationary bulk can penetrate into IDZ along with the aligned AIEZ around the dielectric pillars. The individual AIEZ can be observed not only in the computational map but also in the experimentally visualized map. This is attributed to the inter-pillar convection due to EOF. As shown in Figure 3.3.5 (c) and 3.3.5 (d), the vortices around each dielectric pillar are inter-connected to form an elongated loop. From these observations, we can conclude that the contribution of EOF would be larger in aligned configuration than in staggered configuration.

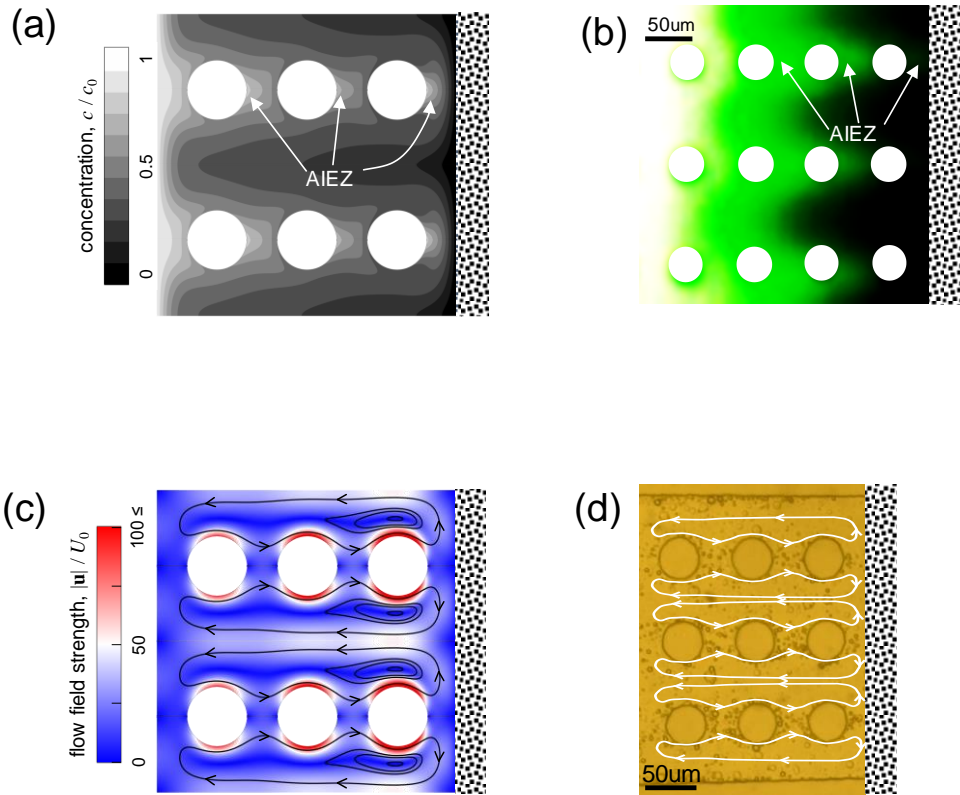


Figure 3.3.5 (a) Numerically simulated and (b) experimental visualized deformed concentration profile of the aligned dielectric pillar configuration. (c) and (d) are the flow field simulation and flow tracking experimental results of aligned configuration, respectively.

3.3.6 Current-voltage characteristics depending on surface charge density and Debye length of the aligned configuration

Similar to staggered configuration, the speed of tracer is accelerated only when it passed around the pillar. From these observations, we presumably conclude that the contribution of EOF would be larger in aligned configuration than in staggered configuration. The tile plots of electrokinetic parameters shown in Figure 3.3.6 reflected this observation. Noteworthy, the contribution of EOF (red dash dot line) is predominant in most cases, while one of SC (blue dot line) is almost identical to the staggered configuration.

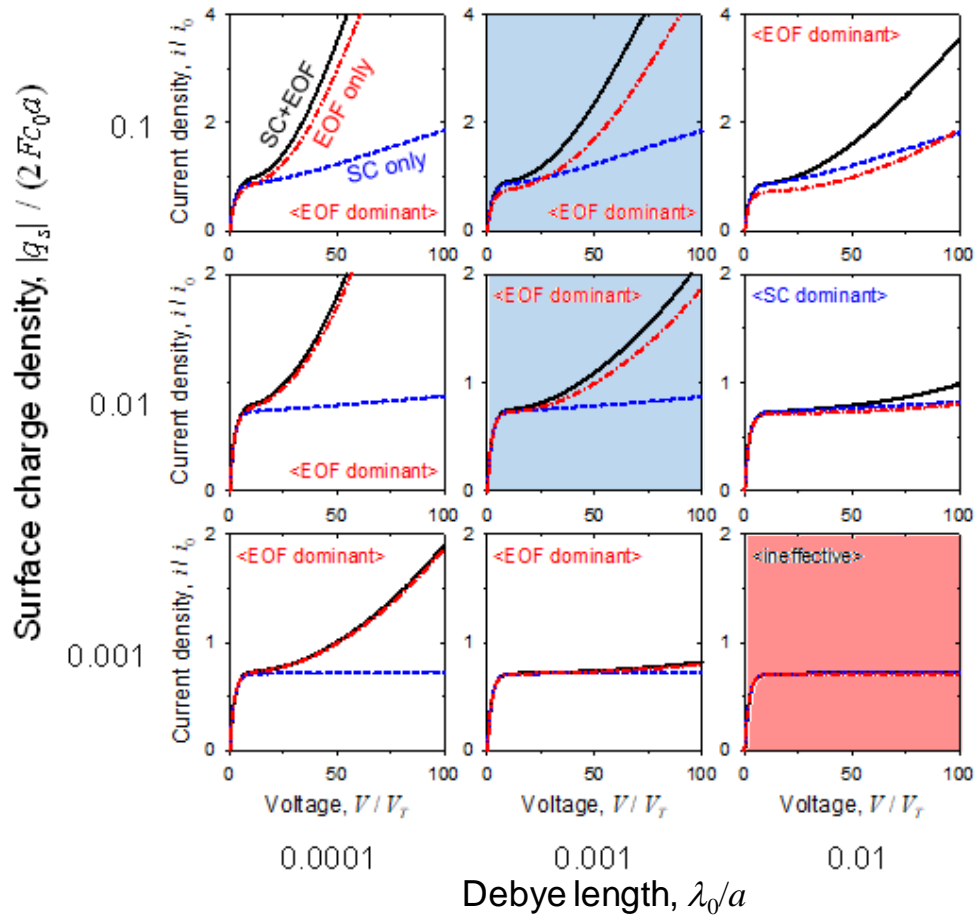


Figure 3.3.6 Current-voltage characteristics depending on surface charge density and Debye length of the aligned configuration.

3.3.7 OLC enhancement by the dielectric pillar

The dielectric microstructures in ED device was expected to be a negative factor that interferes the ion transport because of the current shadow effect and disturbing a convective mixing as mentioned earlier. However, we are expecting significant enhancement of ion transport by the microstructures when the scale of device becomes submillimeter scale. In such scale, SC and EOF mechanism is predominant over EOI. As shown in Figure 3.3.7, the ion transport efficiency (i.e. OLC) significantly increased even though the dielectric pillar array was installed. In this micro/nanofluidic device, where low bulk concentration and high electric field is imposed inside IDZ [44, 45], the dielectric pillar array significantly enhanced the ionic current due to the formation of AIEZ by SC and EOF, meaning this AIEZ conveyed distant ion carriers closer to the membrane. This is directly associated with OLC.

As predicted by Figure 3.3.3 and Figure 3.3.5, aligned configuration had higher EOF contribution, while SC contribution was almost identical in both configurations. This prediction was confirmed in Figure 4 as well. The elongated vortex in the aligned configuration and the localized vortex in the staggered configuration had different charge transfer efficiency to the nanoporous membrane which contributes to OLC differently. Thus, one should carefully consider the physical configuration for high energy efficient electrochemical membrane platform even though the physicochemical parameters such as surface charge of device and bulk electrolyte concentration were fixed.

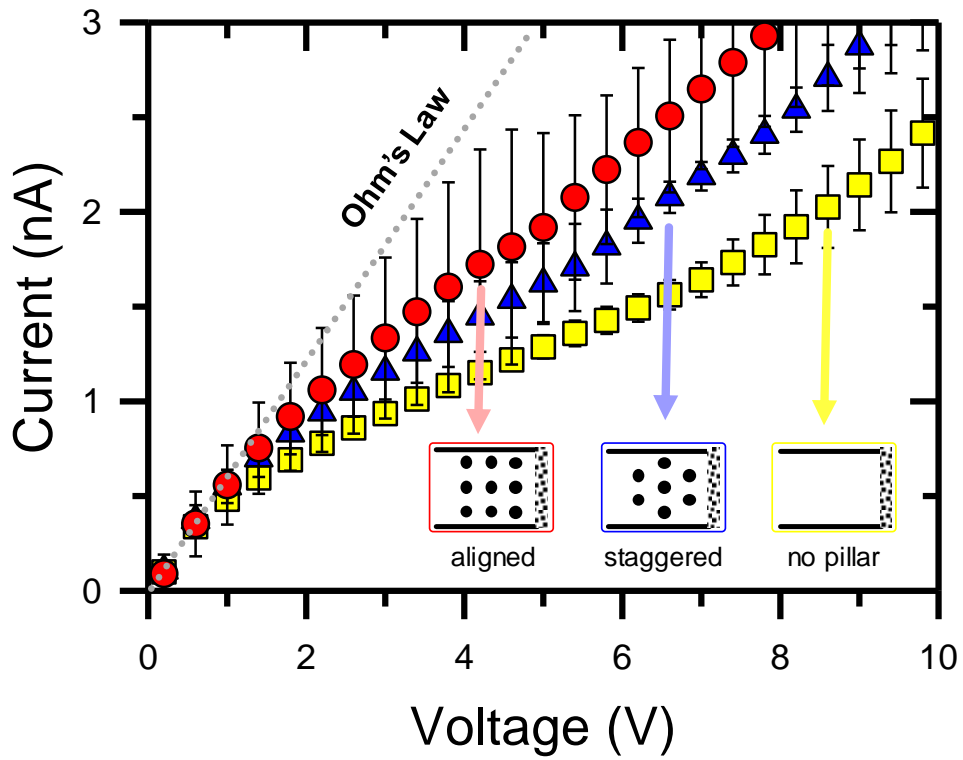


Figure 3.3.7 Experimentally measured current-voltage relations for no pillar (rectangle), staggered (triangle) and aligned configuration (circle).

3.4. Conclusions

Microstructure such as dielectric spacers used in conventional macroscale ED desalination systems have a negative impact on the perm-selective ion transport through nanoporous membrane due to the current shadow effect. The spacers lead to high electrical resistance and, therefore, to worse power consumption because the ions itself do not migrate where the spacers are located. Thus, in this study, we investigated the electrokinetic effects of the dielectric micro-pillar (which mimicked spacers in ED device) in a micro confinement environment by multi-physics simulation and micro/nanofluidic experiments. The microfluidic confinement would enhance the ion transportation since the length scale of such system is typically within the SC or EOF dominant environment, while macroscale ED system is on EOI regime. We numerically and experimentally confirmed that the combined contribution of SC and EOF caused by the dielectric pillars enhances the ion transport to the nanoporous membrane by forming multiple AIEZs, which is directly associated with OLC. Moreover, two alignment type of dielectric pillar array; staggered and aligned configuration, was rigorously investigated for how the physical structure can affect to the ion transportation. While vortical flow is isolated in staggered configuration, it can be elongated in the aligned configuration so that the latter configuration has higher ion transport efficiency, leading to higher OLC. Conclusively, the fundamental findings of the electrokinetic effects of the dielectric pillars in this study teach us that one should consider not only well-

known electrokinetic parameters such as surface charge and bulk concentration but also the physical configuration of micro-confinement. These results would be an effective mean for designing an efficient electrochemical membrane platform including micro/nanofluidic devices.

Chapter 4. Electroosmotic Instability Contribution on Perm-Selective Ion Transport

4.1 Introduction

Electrochemical membrane systems have gained a great attention for its fundamental significance and possible engineering applications such as electrochemical battery and electrodialysis, etc. In the membrane system such as electrodialysis (ED) is, the cation-permeable selective membrane and the anion-permeable selective membrane are alternately disposed used for desalination. And inside this system dielectric spacers are installed between cation- and anion selective membranes in order to prevent any contact and to maintain distance. As we have seen in the previous study, the dielectric pillar structure (which mimicked the spacer in ED system) enhance the ion transportation since the length scale of such system is typically within the SC or EOF dominant environment by forming multiple AIEZs, which is directly associated with OLC. However, in large systems like ED, spacer usually has a negative effect. Although it plays important role in maintaining the inter-membrane distance it occupies its own space, and thus the current shadow effect appears which is directly related to the interruption of current flow as shown Figure 4.1 (a). Therefore, leads to an increase in resistance and therefore to a higher power consumption.

Depending on the characteristic length scale, the driving mechanism of perm-selective ion transportation is categorized into (i) surface conduction

(SC)[36, 51, 52], (ii) electroosmotic flow (EOF)[1, 13, 53, 54] and (iii) electroosmotic instability (EOI)[2, 14, 55-57]. The length scale of typical ED system lies in EOI regime[58] so that reducing convection by spacer would lower the ion transport. So, as expected, we found that OLC was lower when there was spacer array than when there was no spacer as shown in Figure 4.1 (b).

In this study, we aimed to conduct an experimental and multi-physical simulation of mass transport enhancement in macroscale by employing different spacer structures inside the depletion zone. By I-V characterization and imaging of the concentration profiles with spacers in two different patterns, we found that by organizing the spacers in different manners, specific patterned spacers can enhance the charge transport in the unstable electro-osmotic instability dominant regime by suppressing the electro-osmotic instability in systems where it is unwanted and by fixing the electroconvective mixing in each desired location. By properly patterned configuration, we can regularize the electroconvection and were able to enhance the electroconvective mixing efficiency. Therefore, the significant enhance of the net transport led to the increase of the OLC.

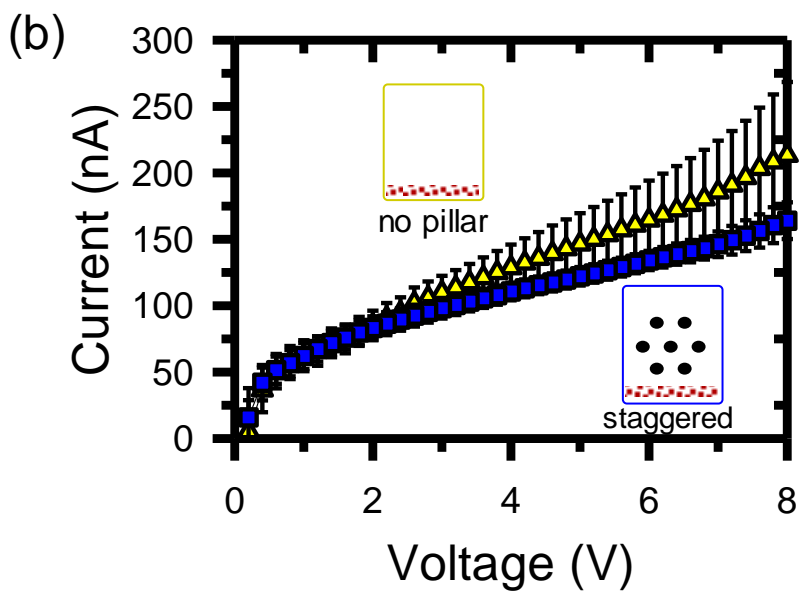
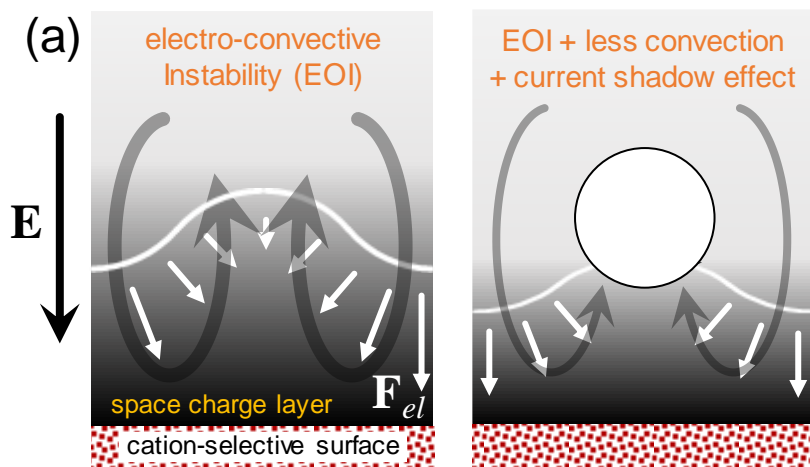


Figure 4.1 (a) Schematic diagram of electro-convective instability (EOI) and the schematic of deformed convection by spacer. (b) Pre-experimentally measured current-voltage relations for no spacer (triangle-yellow) and staggered spacer (square-blue).

4.2 Experimental Setup

To investigate the effect of the spacer, PDMS based spacer array (15 μm radius and inter-pillar distance of 95 μm and 100 μm) were designed inside the main microchannel with two types of configuration (aligned and staggered). On the microchannel, we added side microchannels on both sides of the main- and buffer-microchannel for the repetition of the experiment[67]. The dimensions of the microchannel were as following; the main- and buffer-microchannel: 200 μm width \times 180 μm depth \times 6mm length; the air valve microchannel: 15 μm width \times 180 μm depth. We followed the general soft-lithographical fabrication steps. Briefly, polydimethylsiloxane(PDMS, sylgard 184 silicone elastomer kit, Dow Corning, USA) base was mixed with a curing agent at 10:1 ratio. After pouring the solution onto the master, it was heated in an oven at 75 $^{\circ}\text{C}$ for 4 hours. Cured PDMS piece was peeled off from the master and cut into each device. The device fabrication step is shown in Figure 4.2 (a). Punching out the inlet and outlet holes, razor cutting was performed in the center of the device. As a nanoporous membrane we added Nafion PFSA membrane sheet in the middle of each microchannel using plasma bonding and silicon bonding, considering the aspect ratio of the main channel. Then thin PDMS sheet was bonded by oxygen plasma treatment (Femto Science, Korea) and was heated at 95 $^{\circ}\text{C}$ for 1 hour and after the PDMS substrate was flipped, the slide glass was bonded. The fabricated device is shown in Figure 4.2 (b).

For visualization of the experiments, charged fluorescent dye Alexa Flour

488 (1 μ M, Invitrogen, USA) were used for the observation of the concentration profile.

In the microfluidic experiment, using Ag/AgCl electrodes, external electric field was applied by a source measure unit (Keithley 236, USA). Current-voltage response were cyclically measured in the range from 0 V to 8 V (0V \rightarrow 8V \rightarrow 0V) at ± 0.2 V/30 sec. The current values were automatically recorded at every step by customized LabView program.

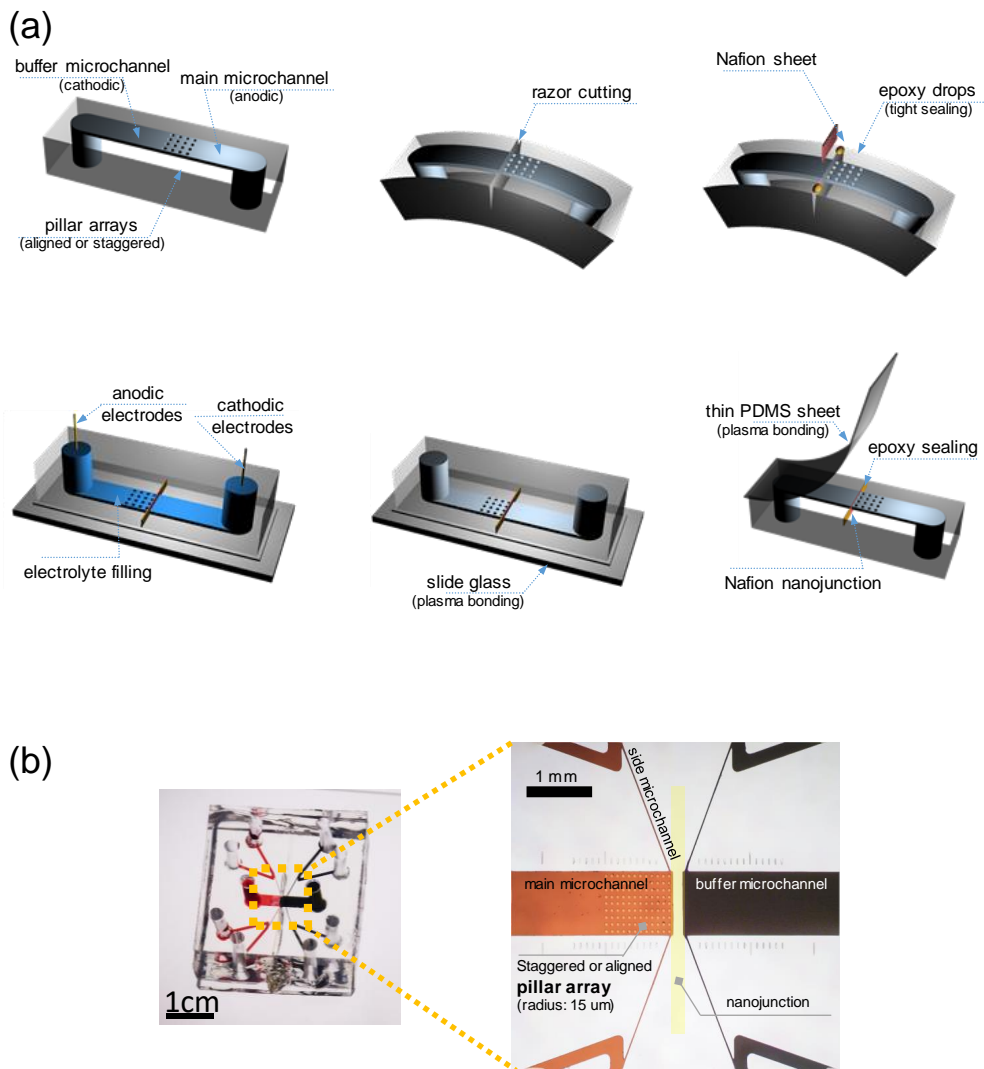


Figure 4.2 (a) Fabrication step of micro/nanofluidic device using Nafion PFSA membrane sheet. (b) Snapshot and microscopic images of fabricated micro/nanofluidic device, integrated with spacer array on anodic side.

4.3 Results and discussion

4.3.1 Concentration profile of spacer array configuration

To investigate the effect of spacers inside the IDZ, electric potential was applied to the main microchannel and the buffer microchannel was grounded so that IDZ is formed at the main microchannel where the spacers were installed. As shown in Figure 4.3.1 (a), the experimental vortex was visualized and simulated of electro-instability by observing the concentration profiles.

The first spacer type is a staggered configuration. The simulation and experimental result of concentration profile inside IDZ are shown in Figure 4.3.1 (b). The concentration gradient inside IDZ in this configuration is randomly deformed (*i.e.* random fingering) near the nanoporous membrane. Visualizing the experimental and simulation result, the convections are suppressed by the spacers that can be a negative effect to the ion transport since the convection which arises as a result of instability of the fluid near the nanoporous membrane is the dominant source of OLC. The second configuration is a structure that is arranged in an aligned pattern. As demonstrated, the visualized and computed concentration profiles were shown in Figure 4.3.1 (c). In this configuration the concentration gradient inside the IDZ is more deformed than the previous configuration, but in an organized form (*i.e.* guided fingering). By this guided fingering, we can expect to enhance the charge transport in the unstable electro-osmotic instability regime by locking up the concentration gradient one by one of the columns.

By this comparison, by properly patterning the configuration structure, we can control the electroconvection and can expect to enhance the electroconvective mixing efficiency

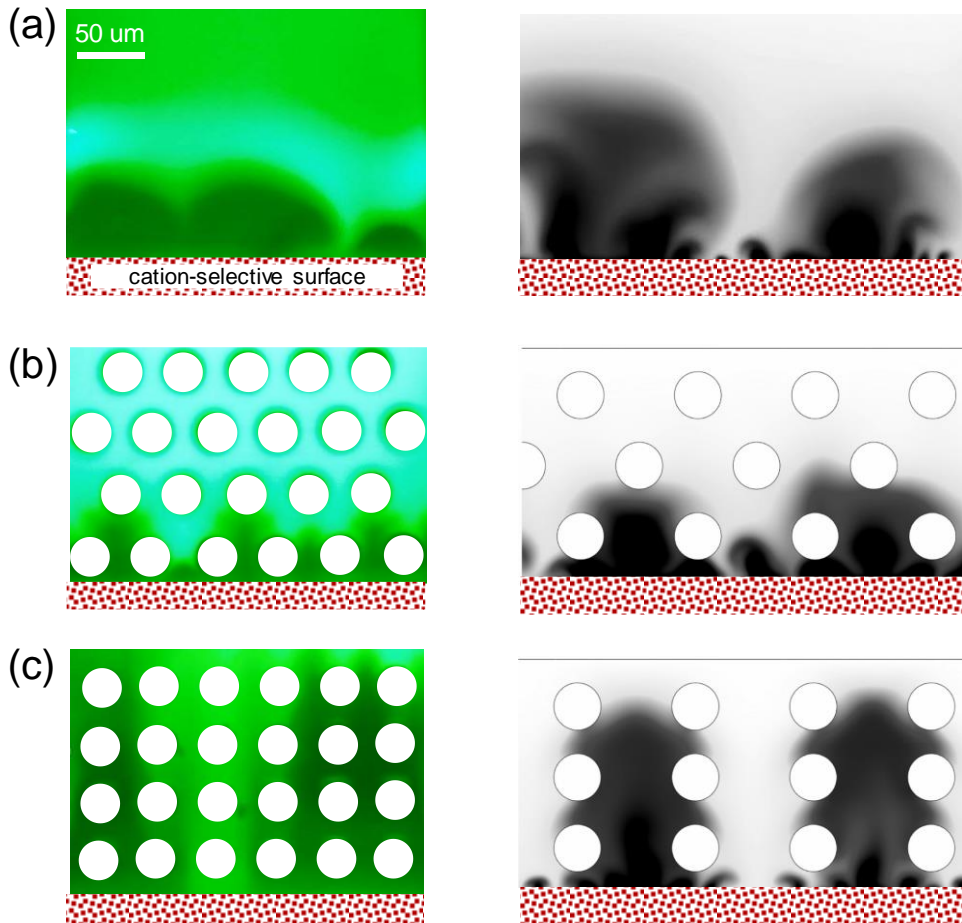


Figure 4.3.1 (a) Experimental visualized and numerically simulated concentration profile of no spacer configuration. (b) and (c) are experimental visualized and numerically simulated concentration profile of staggered and aligned spacer configuration.

4.3.2 Current-Voltage characteristic of spacer configuration

The dielectric spacers in ED device was expected to be a negative factor that interferes the ion transport because of the current shadow effect and suppressing the convective mixing as mentioned earlier. So as expected, we found that the OLC was lower when there was spacer array inside the IDZ in Figure 4.3.2 (a). However, by reorganizing the spacer configuration, which is to confine the electroconvection as shown in previous section, we can expect to control the convection and expect in enhancing the power efficiency. Simulation result shown in figure 4.3.2 (b) shows three configurations (*i.e.* No spacer, Staggered configuration, Aligned configuration) of the current-time graph. With no spacer, the current density is not stable and is vibrating up and down with high amplitude. Adding the staggered configuration spacer array, the current density seems quite stable. However, due to the current shadow effect and the suppression of the electroconvection, the current values are lower than with empty spacers. The aligned configuration spacer array has the highest current value and are even stable as expected due to the significant enhancement of overlimiting transport. To verify the simulation results and to observe the overlimiting current regime, experiment was conducted as in figure xx. As predicted, aligned configuration had the highest OLC values. To compare the stabilization, the standard deviation for each voltage value was calculated and was averaged. Thus, one should carefully consider the physical configuration for high energy efficient electrochemical membrane platform.

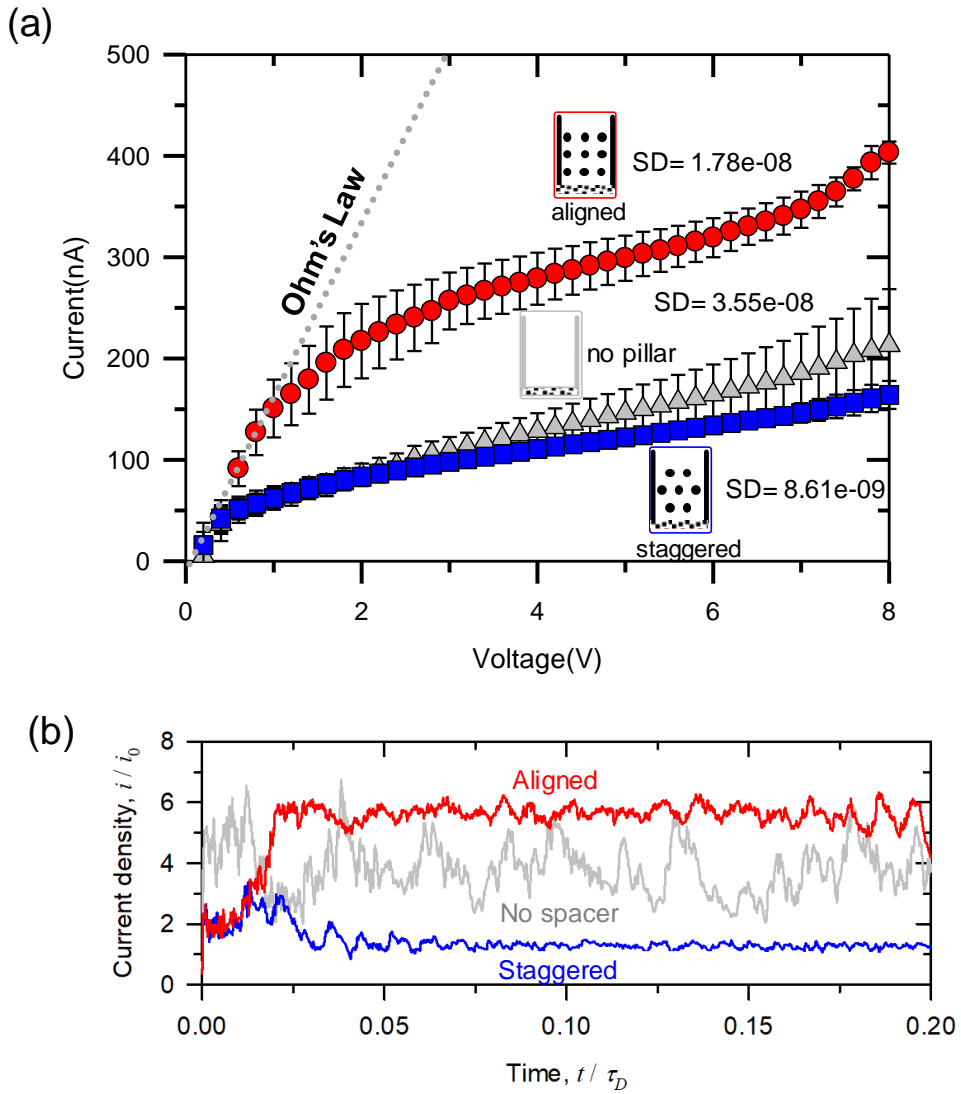
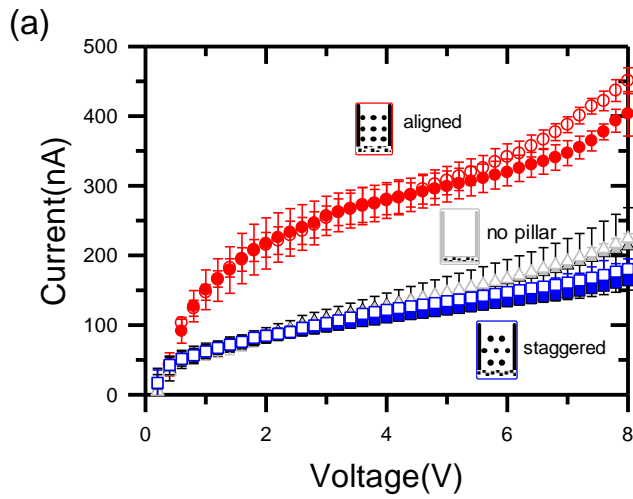


Figure 4.3.2 (a) Simulated results of current-time characteristic of no spacer (gray), staggered (blue) and aligned configuration (red). (b) Experimentally measured current-voltage relations for no spacer (triangle-gray), staggered (rectangular-blue) and aligned configuration (circle-red).

4.3.3 Surface charge of spacer configuration

For the electro-osmotic instability regime, as the channel thickness is increased further, this causes instability in specific condition. The main point here is that the surface charge of the spacers creates a competition between the instability and the EOF of the spacer. When the surface charge density of the spacers is high $U_{EOF} \gg U_{instability}$ is formed and therefore suppress the instability. When the surface charge density of the spacer is low $U_{EOF} \ll U_{instability}$ is formed and therefore grows the instability. The growth of the instability is the main reason for the growth of the current because the mixing efficiency is better than the electric field applied.

To be more specific, BSA coating was applied to the device to lower the surface charge of the entire system. The current value increased slightly. Shown in Figure 4.3.3 (b), we can see not much difference in the OLC. To confirm the experimental result, by numerical simulation shown in Figure 4.3.3 (c), at a certain point, the instability grows as the surface charge density is low and the instability is suppressed as the surface charge density is high. As to compare with the simulation results shown in Figure 4.3.3 (c), OLC was slightly higher with the BSA coating.



(b)

	No spacer	Staggered	Aligned
w/o BSA	2.73E-08	1.72E-08	5.23E-08
w/ BSA	3.16E-08	1.90E-08	6.16E-08

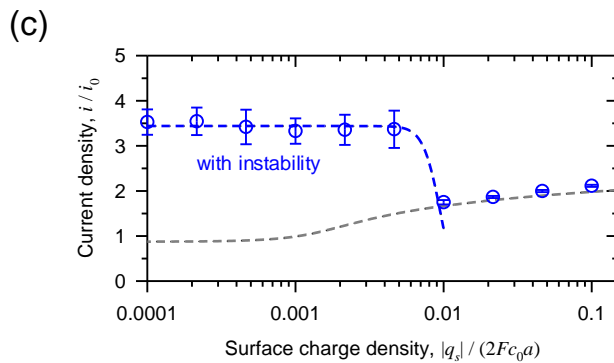


Figure 4.3.3 (a) Experimentally measured current-voltage relations for no spacer (triangle-gray), staggered (rectangular-blue) and aligned configuration (circle-red); Color not filled indicate BSA coating was applied to the device. (b) Table of overlimiting current (OLC) value in Figure 4.3.3 (a). (c) Simulated results of current density depending on surface charge density of spacer

4.4 Conclusions

Dielectric spacers in the membrane system such as ED desalination systems usually have negative effect due to the current shadow effect which leads to high resistance and therefore has a negative impact on the ion transport through the nanoporous membrane. Therefore, in this work, we investigated on the effects of the spacer array configuration by multi-physics simulation and micro/nanofluidic experiments of how to enhance the ion transport by employing different spacer structures inside the depletion zone. The device length scale lies on EOI regime, and therefore the spacers itself suppress the electroosmotic instability and therefore reduce the convection which lowers the ion transport. However, by reorganizing the alignment type of the spacer array from staggered to aligned configuration, we were able to enhance the charge transport in the unstable electro-osmotic instability dominant regime by suppressing the electro-osmotic instability in systems where it is unwanted and by regularizing the electroconvection in each desired location. We verified the effect of the physical configuration by evidence by analyzing the concentration profile and through I-V characteristics of each configuration. These results would play a guiding role for designing an efficient electrochemical membrane platform including micro/nanofluidic devices.

Chapter 5. Conclusions

In this thesis, we experimentally investigated the electrokinetic responses inside and outside of the depletion zone during ICP phenomena by changing the geometry structure of the microchannel and also by installing microstructures inside the depletion zone.

In *Chapter 1*, the introduction was presented by explaining the background of Ion Concentration Polarization (ICP) and a brief review of ion transport. The concentration profile, particle tracking, and the electrical response were investigated. In *Chapter 2*, a micro/nanofluidic device for preconcentration and separation of two charged molecules with different physicochemical properties based on ion concentration polarization was proposed. With the balance of electroosmotic drag force and electrophoretic force on the molecules, they were highly preconcentrated and separated simultaneously. Due to the sporadic electric field distribution new design of repeated microchamber structure was installed. By the geometry effect, the electric field was focused on the narrow channel and therefore ion depletion zone was stabilized and plugs were well-defined. For subsequent on-chip or off-chip application, pneumatic microvalve system was integrated and selectively preconcentrated. In *Chapter 3*, we provided evidences on how SC and EOF around the dielectric microstructures can accelerate the ion transportation by multi-physics simulations and direct visualizations. Additional ion enrichment zones (AIEZ) were formed on each microstructure inside an ion depletion zone so that AIEZs can directly bridge

ion carriers from bulk to the nanoporous membrane. Furthermore, we verified that the physical configuration of a micropillar array has a critical impact on SC and EOF which has been typically neglected. *In Chapter 4*, we investigated on the effects of the spacer array by micro/nanofluidic experiments and simulation. The study was conducted on how to enhance the ion transport by employing different spacer structures inside the depletion zone. The device scale lies on EOI regime, and therefore the spacers itself suppress the electroosmotic instability. However, by rearranging the alignment type of the spacer, we were able to enhance the charge transport in the unstable electro-osmotic instability dominant regime by suppressing the electro-osmotic instability in systems where it is unwanted and by regularizing the electroconvection in each desired location. Given the importance of the analytical approach based on experiment results, we expect that this thesis would play a guiding role for designing structures for an efficient permselective micro/nanofluidic membrane device.

Appendix

A. Laminar flow assisted anisotropic bacteria absorption for chemotaxis delivery

This experiment was conducted by Keon Huh and Darong Oh who now belongs to Samsung Electronics.

In Appendix A, we proposed a simple, but effective microfluidic structure for anisotropical absorption of bacteria to microparticles for demonstrating bacteria integrated microrobot. By flowing attenuated *S.typhimurium* bacteria into the microfluidic channel, hydrophobicity of microparticles made of biodegradable polycaprolacton (PCL) enabled a quick bacterial absorption (<100 seconds) without any toxic adhesive substance or chemical modification. Moreover, the bacteria were attached only at the surfaces of microcubics facing against the flow direction and the rest of the surfaces were free from the absorption, since Laminar flow can eliminate any backflow or vortical flow. The maximum motility of the bacteria-attached microparticle was measured to be ~5 um/sec ($E_k=58.952\times 10^{-21}$ J) by chemotaxis which is comparable to prior state of art technologies.

Appendix A.1. Bacteria culture

The random speed and motions of bacteria are controlled by the taxis characteristics [68]. Among various taxis mechanisms, chemotactic characteristics have been recently studied [69] because a target site (*e.g.* cancer site) often released a specific chemical for bacteria to be followed. *S.*

marcescens and *S. typhimurium* especially shows the directional movement toward chemo-attractant by flagella motor [70, 71]. Bacteria used in this work were attenuated *S. typhimurium* (SHJ2037) since it has chemotactic behavior toward a breast cancer site and also has shown a reasonable safety level by several clinical trials [72]. In addition, the attenuated *S. typhimurium* is characterized by fluorescence expression for easy tracking of their movements. *S. typhimurium* were inoculated in solid Luria-Bertani broth medium (LB medium) consisted of 500 mL DI water, 7.5 g agarose powder (DUKSAN, Korea), 5 g sodium chloride (NaCl, DUKSAN, Korea), 5 g tryptone (Becton, Dickinson and Company, USA) and 2.5 g yeast extract (Becton, Dickinson and Company, USA). The solid LB medium was incubated at 37 °C for overnight since it is easier to get highly active bacteria in solid LB than in liquid LB. From the inoculated solid LB medium, one bacterial colony was picked and cultivated in the 10mL of liquid LB medium that contained 50 ug/mL of Kanamycin and Ampicillin. Then the bacteria was incubated at 37 °C on shaking incubator at 120 rpm for 3 hours. The engineered *S. typhimurium* at an optical density (OD₆₀₀) of 1.0-1.5 (UV/VUIS Spectrophotometer-Optizen 2120 UV, Mechasys, Korea) were used in this experiment.

Appendix A.2. Experimental setups

Main microfluidic channel of device was connected with syringe pump (Harvard PHD 2000, USA) using four-port switching valve (IDEX, USA) for sequential injection and the outlet channel was linked with another syringe pump. First, the mixture of microparticles (100 ea./mL) was diluted with

dimethyl sulfoxide (DMSO, DAEJUNG, Korea) and injected into the device at a flow rate of 0.1 mL/min for 10 minutes. DMSO reduces friction between microparticles and the surface of channel. Since DMSO has toxicity to bacteria, DI water was injected to wash out DMSO. After DMSO was completely removed, *S. typhimurium* was pumped into main channel at 3 uL/sec. The hydrophobicity of microcubics made of biodegradable PCL enabled a bacterial absorption without any adhesive substance or chemical modification. Moreover, the bacteria can be attached only to the surfaces of microparticles facing against the flow direction and the rest of the surfaces were free from the absorption. Lastly, back-pressure from the outlet channel was applied into the main channel for releasing and collecting the bacteria-attached microparticles. All of experiments were monitored with IX51 inverted fluorescent microscope (Olympus, Japan) and the images were post processed using CellSens software (Olympus, Japan).

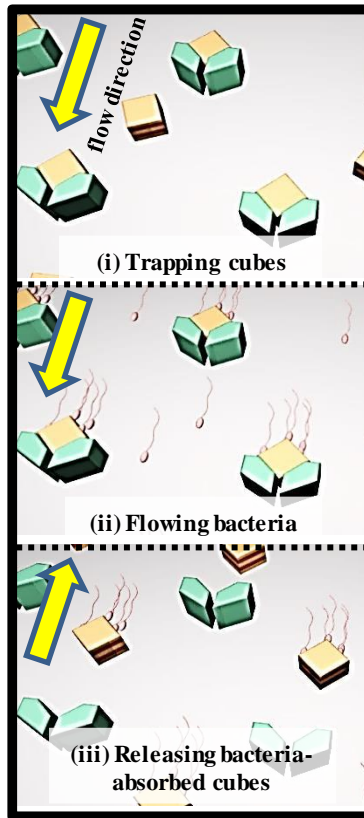
Aforementioned *S. typhimurium* was attracted by aspartate acid [73]. For evaluating the chemotactic motility, we used 10 mM of α -methyl-DL-aspartic acid (Sigma-Aldrich, USA) solution as a chemo-attractant in the flow-free microfluidic channel. The concentration of attractant was chosen as previous studies.[73, 74]. Before the demonstration using the microparticles, the chemotaxis of *S. typhimurium* itself was tested in Y-shaped microchannel. The bacteria were injected from the left reservoir and 10 mM of aspartic acid was dropped only at bottom right reservoir. Note that bacteria were able to be moved only by diffusion since there was no net flow from anywhere. However, the bacteria tended to move toward the bottom right reservoir and there was no

reason for this movement except the chemotaxis.

Appendix A.3. Microfluidic trapper for anisotropic bacterial absorption

The main concept of the fabricating bacteria-attached microparticle is shown in Appendix Figure A.3. We designed micro-structures called “trapper” to hold the microparticles for anisotropic attachment of the bacteria. The trappers play a role as structural blocker so that they allow the bacteria attachment to the surfaces of micro-cubes facing against the flow direction and, thus, the rest of the surfaces were free from the absorption. Bacteria-attached microparticle production method using the trappers is as follows. First of all, the fluid contained microparticles are injected from the top and they are caught in trappers (Appendix Figure A.3-(i)). The shape of trapper is designed to capture only one microparticle and residual cubes automatically flow down toward the next trapper to fill the entire array of the trappers. Next, bacteria are injected for a while from the top as well. The duration and flow rate will be discussed later on. Because microparticle made of PCL polymer has hydrophobic surface [75], these surfaces adsorb bacteria without any additional chemical or physical treatments (Appendix Figure A.3-(ii)). Excess amount of bacteria is supplied by fluidic flow to the microparticles for conformal absorption, while previous studies usually have attached the bacteria in static conditions (*i.e.* without any flows). Laminar flow helps to prevent undesirable attachment to the backside surface of microparticles. Finally, bacteria growth medium is pumped into the channel in the opposite direction Appendix Figure A.3-(iii)). The stream is capable of releasing the captured microparticles by

fluidic inertia and they are collected at the top inlet reservoir. Thus, our unique method has several advantages; (1) simple production with low cost due to the absence of additional chemical or electrical treatments, (2) reusability of the device since severe washing steps are not involved in this concept and (3) high scalability because one can expand the size of arrays as long as low Reynolds fluidic regime is satisfied.

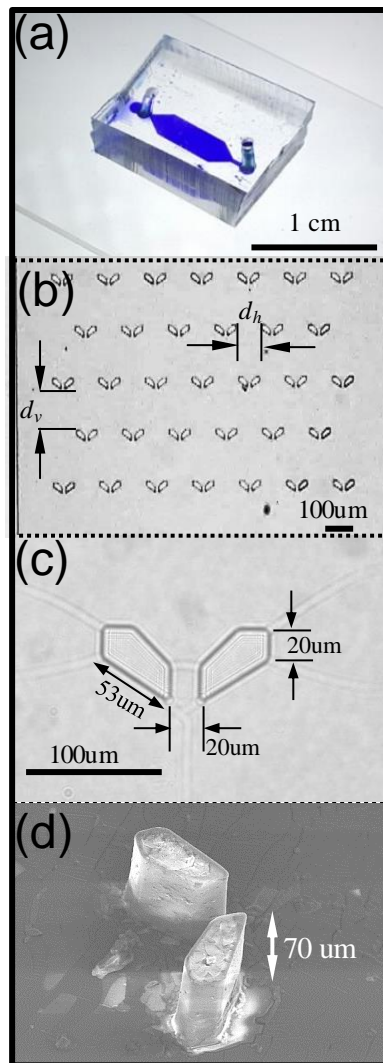


Appendix Figure A.3 Adsorption concept for anisotropic bacteria attachment.

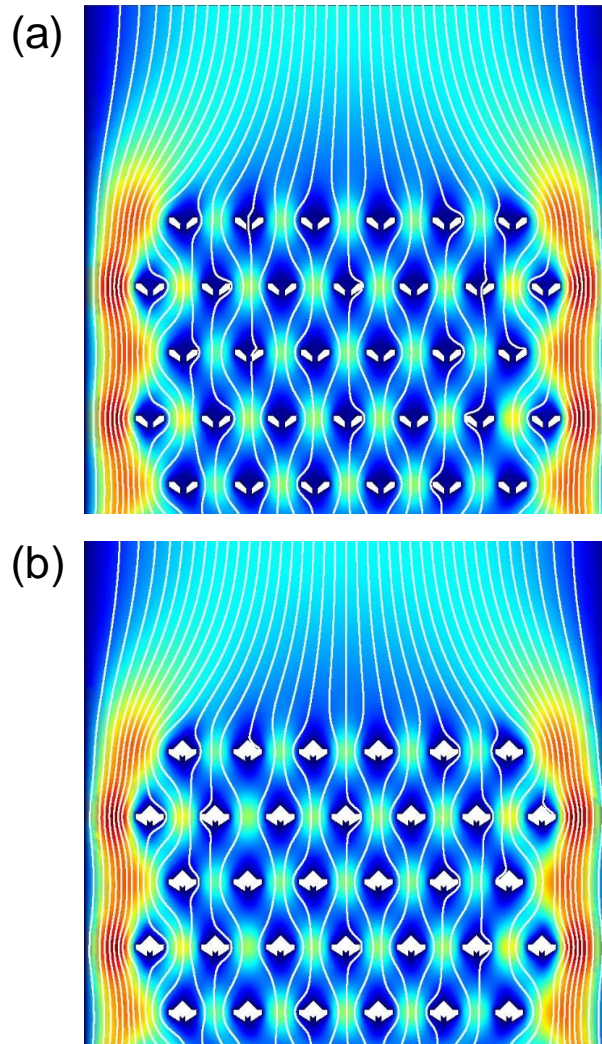
Appendix A.4 Microfluidic trapper device

A simple straight channel device including trapper arrays in the middle was designed and fabricated as shown in Appendix Figure A.4(a). The height of the channel was 40 μm or 70 μm for microparticles of 30 μm X 30 μm or 50 μm X 50 μm , respectively. The height was larger than the size of microparticle for smooth flowing through the channel without clogging or stacking. The width of the channel was 2.0 mm or 2.5 mm for arranging 7-6 or 14-15 trappers in one line (Appendix Figure A.4(b)). The detailed shape of trapper was chevron with small gap in the middle as shown in Appendix Figure A.4(c) and 3-dimensional SEM image was shown in Appendix Figure A.4(d). The gap between the trapper arms decreased fluidic resistance to assist comfort landing of microparticles. The horizontal (d_h) and vertical (d_v) distance between each trapper were adjusted depending the size of microparticles. d_h was set to be 140 μm (in the case of 50 μm X 50 μm microparticle) for preventing unwanted stacking of microparticles between trappers. d_v was determined to be 200 μm (in the case of 50 μm X 50 μm microparticle) through analyzing data using COMSOL multiphysics. As shown in Appendix Figure A.4.1(a) and Appendix Figure A.4.1(b), this microfluidic device has a low Reynold number regime so that all streamlines persist a laminar flow, *i.e.* the microparticles followed the streamline for consecutive trapping from the top trapper. U_0 was the inlet velocity of sample flow. However, the microparticle had significant mass so that an inertia effect drove the microparticle to fall down straightly toward the next trapper. Likewise, the microparticle went around the occupied trapper,

seeking unoccupied trapper. As a result, each trapper possessed only one microparticle, filling the entire array 1 by 1. Maximum velocity appeared at the sides of channel will be discussed later on. Bacteria also followed the laminar streamline to approach to the microparticle. Since excess amount of bacteria were supplied from inlet reservoir, there was a higher stochastic chance for the bacteria to contact the microparticle surface than no flow condition in previous literature. However, the flow rate should be carefully determined since the bacteria should stay around the cube for the residence time (*i.e.* the time requires for the absorption.)



Appendix Figure A.4 (a) Fabricated device, (b) microscopic image of the trapper array, (c) magnified view for 50 μm microcube trapping and (d) SEM image of the trapper. Horizontal (d_h), vertical (d_v) distances and height of trapper were varied depending on the size of microcubes, while the dimension of trapper itself was fixed.

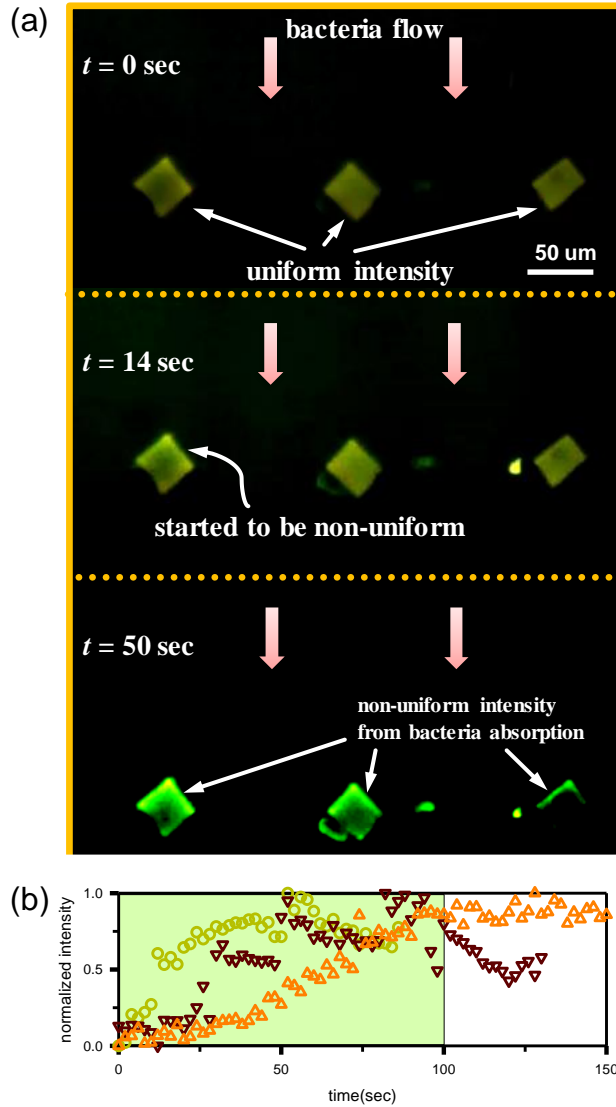


Appendix Figure A.4.1 Numerically simulated streamlines and velocity magnitude contour plots of (a) before and (b) after capturing microcubes. Reynolds number was set to be 1. The velocity has the maximum values near both walls of microchannel.

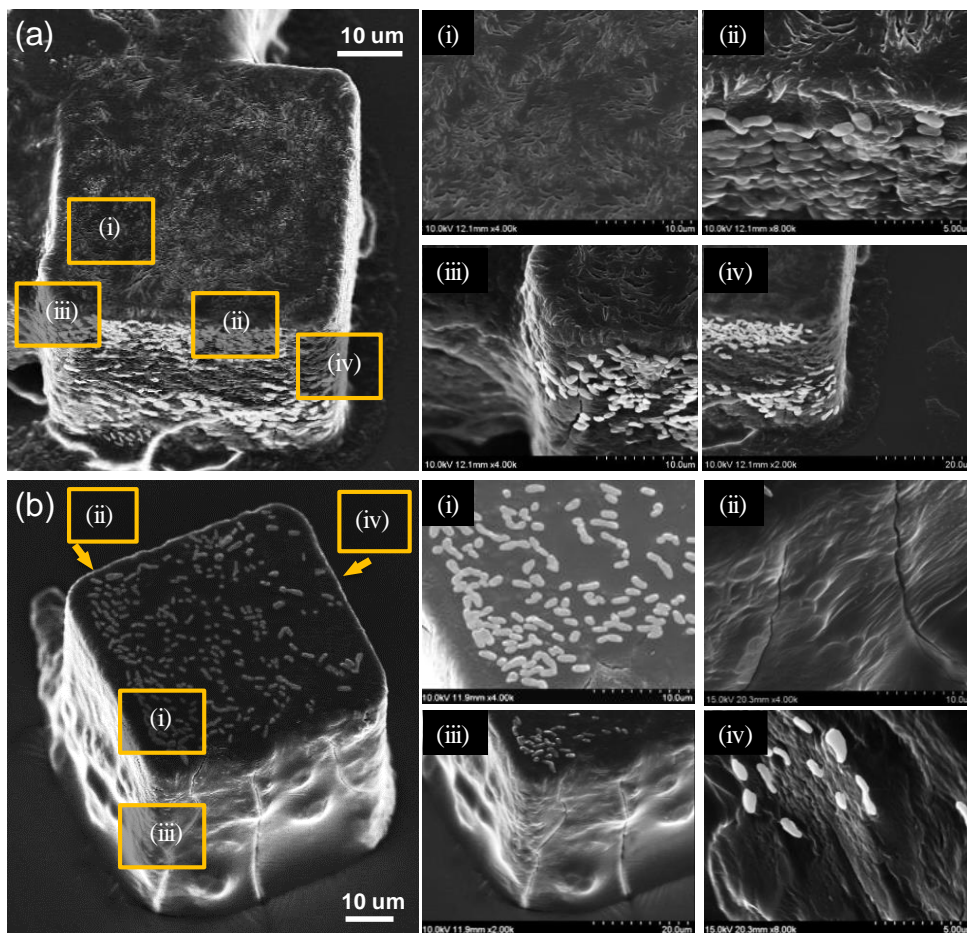
Appendix A.5. Anisotropic bacteria absorption

After the microparticles filled the trapper array, GFP labeled *S. typhimurium* were injected from the top. Appendix Figure A.5(a) showed the snapshots during the absorption process. At first, three captured microparticles (30 μm X 30 μm) had almost uniform fluorescent intensity. Since the bacteria collided and were absorbed only to the two surfaces facing against the bacteria flow, the intensity of the surfaces became brighter than remaining surfaces. The intensity of the first cube started to be non-uniform from 14 seconds. After 50 seconds, the intensity was saturated. Therefore, the dynamics of absorption was a fast (or linear) absorption at the initial and saturation after a while (the graph of Appendix Figure A.5(b)). Randomly selected 3 different experimental sets (with the same experimental conditions) among a number of analysis were shown as a function of time and they followed the dynamics. We found that the saturation time for the anisotropic attachment was at most 100 seconds from all analyzed data sets. Compared to previous studies that took at least 5 minutes for attaching bacteria, for example, *S. marcescens* [76, 77] and *V. alginolyticus*[78], even more than 30 minutes for *S. typhimurium* [79, 80], our laminar flow assisted method enabled faster attachment than any previous results which relied only on a random motion based (or diffusion based) attachment. Direct evidences of the anisotropic attachment to 50 μm X 50 μm microparticle were provided using SEM as shown in Appendix Figure A.5.1. Magnified view of various locations of the bacteria attached were shown as indicated (i) ~ (iv). The contrast of bacteria was adjusted for clear visualization. They clearly showed that the bacteria were selectively attached at the front/left

surface and the top/right surface. Counting the number of bacteria provided the number density of 0.3 ea./ μm^2 and 0.11 ea./ μm^2 from each image, leading to the surface coverage of 60 % and 25 %. The maximum number density should be limited to 0.5 ea./ μm^2 since the size of bacteria is approximately 1 μm X 2 μm . These results were comparable to the state of art results, for example 0.089 ea./ μm^2 and 0.1 ea./ μm^2 using *S. marcescens* [81-83], respectively. But, more efficiently, our methods achieved the results even without any toxic chemical processes during the absorption and with faster attachment time less than 100 seconds than previous studies.



Appendix Figure A.5 (a) Fluorescent microscopic images of anisotropic bacteria absorption at 30 μm X 30 μm microcubes. Uniform fluorescent intensity at the initial became non-uniform during the bacteria flow was being introduced from the top. (b) Saturation of fluorescent intensity at the site where the bacteria were absorbed.



Appendix Figure A.5.1 SEM images of microcubes (50 μm X 50 μm). The bacteria were selectively absorbed at (a) front/left surface and (b) top/right surface. Inset (i) ~ (iv) showed the magnified image of various surfaces that confirmed the anisotropic absorption.

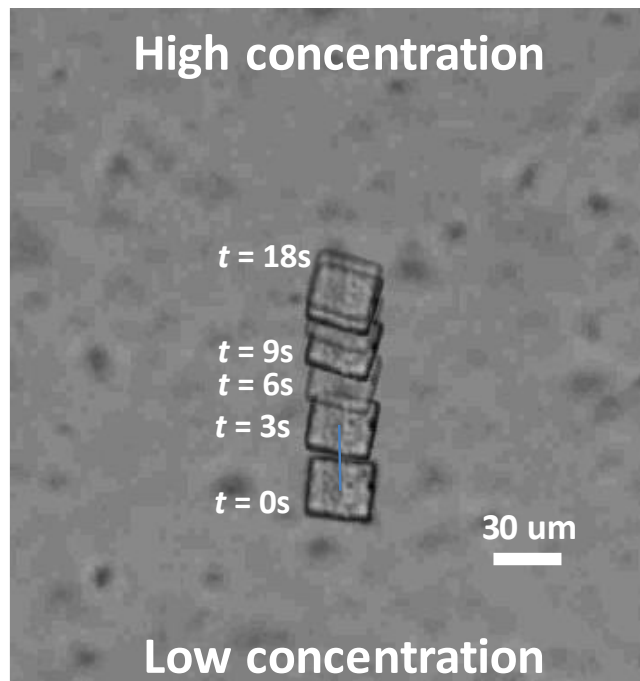
Appendix A.6. Chemotaxis test of bacteria-attached microparticle

Chemotaxis test of bacteria-attached microparticle. *S. typhimurium* that was utilized in this work has chemotaxis toward the concentration gradient of an appropriate attractant. For measuring chemotactic velocity of microparticles, we used 10mM aspartic acid as previous studies used[73, 74]. One representative demonstration was shown in Appendix Figure A.6 and the attractant was dropped on upper area of solution and the microparticle started to move in the direction of the concentration gradient. Images were captured every 3 seconds and it revealed that the microparticles initially moved at 10 $\mu\text{m}/\text{sec}$ and decelerated. The average velocity was measured to be 5 $\mu\text{m}/\text{sec}$. The speed become zero and this is the critical evidence of no-residual flow. Slow down happens when the driving force become lower. A constant concentration gradient is applied for the driving force in a practical chemotaxis. However, the gradient became flat due to diffusion of one-time injected aspartic acid and thus, the traveling distance in this work was only 120 μm . This distance would be extended in a practical chemotaxis since there would be a constant concentration gradient. The particle was initially placed in quiescent solution inside a 5 cm-diameter petri-dish. In such case, Reynolds number is over 100 and a residual flow, if exists, should be oscillating flow due to high inertia force. Thus, the particle must move back and forth under a residual flow, if exists.

While this velocity value was considerably faster than previous bacteria-attached microparticle, one needs to have set up a proper measure, since previous studies had employed different mass (or size) of microparticles.

Kinetic energy

($E_k=0.5mv^2$) would be the candidate to investigate the efficiency of bacteria-attached microparticle. Larger mass could reduce the velocity, but could have higher E_k value. Our presenting *S. typhimurium* attached microparticle has E_k of 58.952×10^{-21} J which is more efficient to other studies mentioned in introduction section.



Appendix Figure A.6 Microscopic images of bacteria based microrobot movement. It moved in the direction of chemical concentration gradient. The images were captured every 3 seconds and overlaid.

Appendix A.7. Conclusions

Laminar flow assisted anisotropic attachment of *S. typhimurium* flagellated bacteria to the microparticles were demonstrated for a chemotactic delivery. A low cost and scalable microfluidic device was designed to trap microparticles and controlling flows upwardly/downwardly enables an anisotropic attachment of the bacteria. Direct visualizations using fluorescent intensity and SEM imaging were performed the attachment and it was measured to be less than 100 seconds to complete the absorption. Chemotaxis test revealed that the maximum velocity of the bacteria-attached microparticle was ~ 5 $\mu\text{m}/\text{sec}$ which is comparable to the state of art researches. Besides, this method excludes any toxic fabrication steps or chemicals so that the devices is reusable. Therefore, the presenting method is highly useful for a chemotaxis delivery of microparticles such as drug delivery system if the microparticles contains a drug.

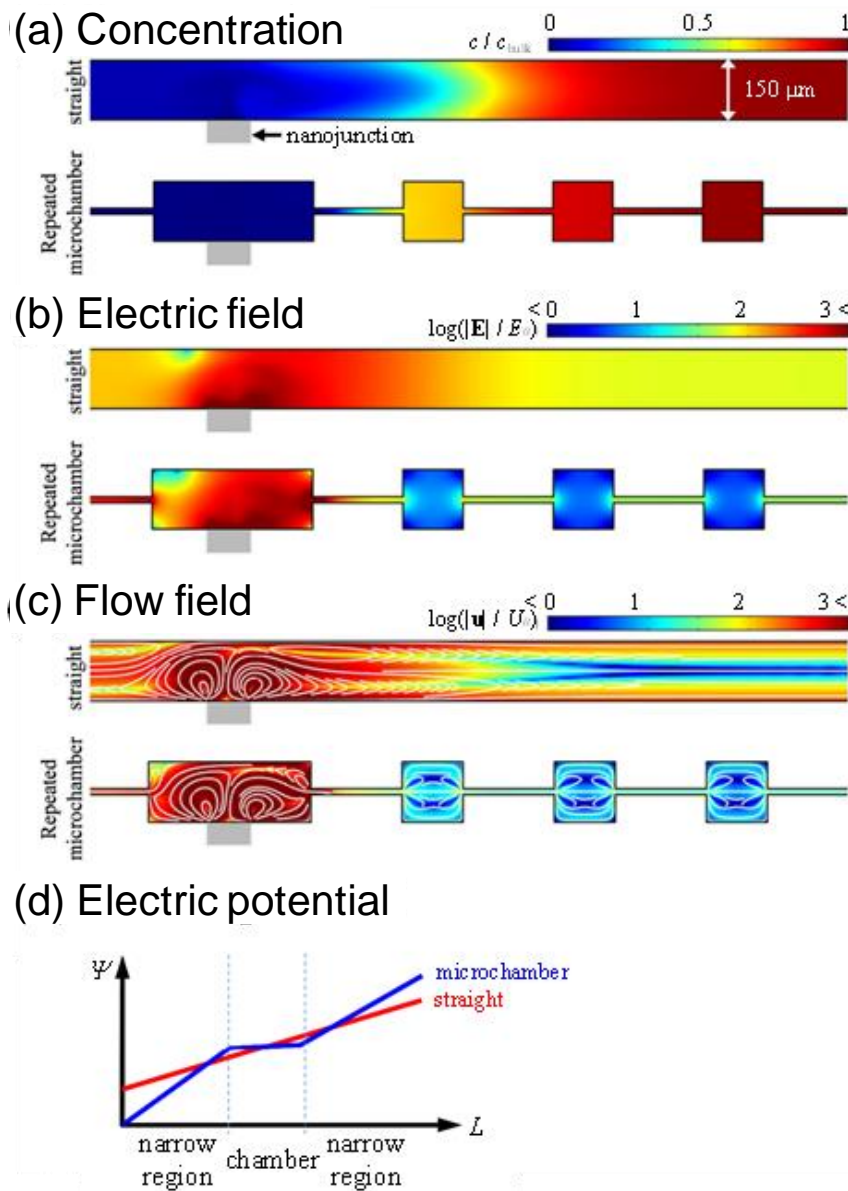
B. Governing equations and boundary conditions for dielectric pillars inside the ICP layer

Prof. Hyomin Lee who belongs to Department of Chemical and Biological Engineering in Jeju National University conducted numerical analysis of ICP layer for straight and repeated chamber structure in chapter 2.

For investigating the effect of repeated chamber structures, numerical simulations were conducted by COMSOL Multiphysics 4.4 as a commercial FEM (finite element method) tool. Because the ICP layer is highly nonlinear region, it is difficult to ensure the convergence and the stability of numerical solutions. To resolve the critical problem, the local electroneutrality (cation concentration is equal to anion concentration in whole domain) was adopted.[84] Namely, thin double layer approximation and ideally cation-selective membrane were chosen to reduce the computational cost. Under the local electroneutrality constraint, independent variables such as ion concentration (c), electric potential (ψ), pressure (p), and flow fields (\mathbf{u}) were governed by the diffusion-convection equation, the current conservation, the continuity equation, and the Stokes equations.[11] ICP phenomena in a straight channel (4 mm in length and 150 μm in height) and a repeated chamber structure (using same geometry of experiments) were analyzed by the governing equations. For the numerical stability, the voltage configurations at inlet and outlet were set to be 5 V and 3.3 V which were enough to generate the ICP phenomena inside the microchannels. The concentrations at inlet and outlet were fixed to the bulk concentration. The flow conditions at the boundaries

were set to be a zero-flow rate due to pressure balance between two reservoirs.[85] We assumed that the microchannel walls have uniform zeta potential of -100 mV of which value is usual condition on PDMS surface.[86]

The simulation results were depicted in Appendix Figure B. First of all, the repeated chamber structures are able to effectively confine the ion depletion zone (dark blue region) in comparison to the straight channel as shown in Appendix Figure B (a). This means that the ICP layer in the repeated chamber would be stabilized because the flow instability generated by concentration fluctuation[7] occurs only inside the first chamber where nanojunction was installed. This is helpful to obtain the stable preconcentrated plug after the first chamber. As depicted in Appendix Figure B (b), the strength of electric field was changed monotonically in the longitudinal direction of the straight channel while the strength was altered pseudo-periodically for the repeated chambers. Electric potentials obtained from the electrical field strength were schematically illustrated in Appendix Figure B (d). While monotonically increased electric potentials were observed in straight microchannel (red line), there was a (almost) plateau inside microchamber with steep changes in narrow regions (blue line). A charged species would be immobilized in this plateau region. Due to the pseudo-periodic electric field and the plateau of electric potential, the preconcentrated plug would be easily trapped in each chamber. Lastly, fast vortices were confined in the first chamber so that stable flow fields were generated beyond the chamber (Appendix Figure B (c)). Thus, the alterations of ICP layer by the repeated chambers would provide effective mechanisms for a stable selective preconcentration.

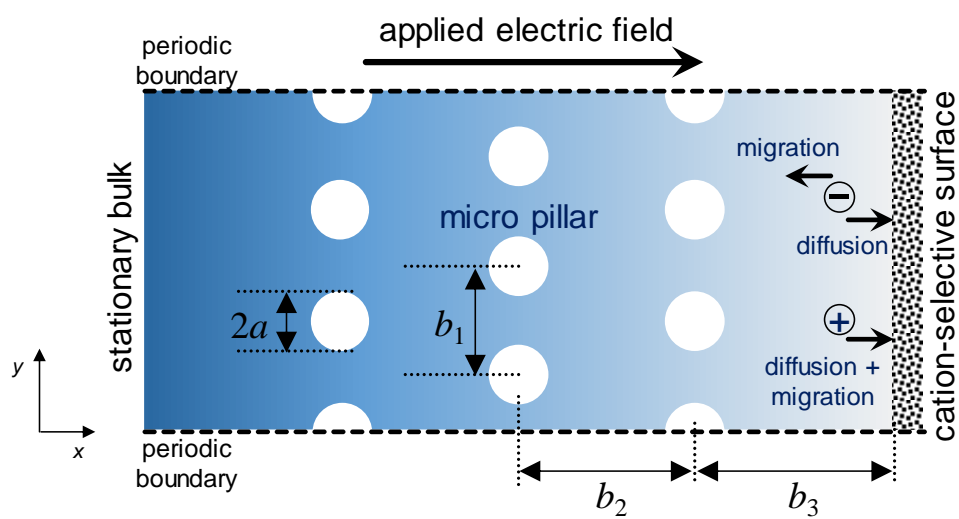


Appendix Figure B Numerically simulated ICP layer for (a) concentration distribution, (b) electrical field and (c) flow field. (d) Schematic illustration for electric potential near the microchamber.

C. Governing equations and boundary conditions for dielectric pillars inside the ICP layer

Prof. Hyomin Lee who belongs to Department of Chemical and Biological Engineering in Jeju National University conducted numerical simulation in Appendix C.

Numerical domain. The microfluidic confinement membrane system with micro dielectric pillars can be represented as a schematic domain as shown in Appendix Figure C. When an electric field is applied across stationary bulk to cation-selective surface, the direction of electro-migrations are different for cation and anion, but anions are not replenished from the opposite side of the membrane. Thus, the total salt concentration in the vicinity to the anodic side of membrane would be largely depleted to form an ion depletion zone (IDZ) and the concentration at the cathodic side would be enriched to form an ion enrichment zone (IEZ). This polarization across the membrane is called ion concentration polarization (ICP) [9, 87]. Note that the same phenomenon is called concentration polarization when the phenomenon is occurred in larger length scale. Dielectric pillar array (diameter = $2a$ and inter-pillar distance is b_1 in y -direction and b_2 in x -direction) is installed apart from the cation-selective surface at b_3 . The cation-selective surface is assumed to have an ideal perm-selectivity so that only cation-flux can pass through



Appendix Figure C Schematic domain of electrochemical membrane system with dielectric pillar array.

Governing equations and boundary conditions. In order to simultaneously calculate ICP and surface conduction/electroosmotic slip on dielectric pillars, we employed the boundary layer model established by Bruus et. al. [88]. Referring to their work, this section briefly introduced the boundary layer model.

The dimensionless ion concentration, c and dimensionless electric potential, ϕ were governed by

$$\nabla^2 c - Pe^0 \nabla \cdot (c \mathbf{u}) = 0 \quad (1)$$

$$\nabla \cdot (c \nabla \phi) = 0 \quad (2)$$

where Pe^0 is the material Peclet number. Pe^0 was defined by

$$Pe^0 = \frac{\tilde{\varepsilon} \tilde{V}_T}{\tilde{\eta} \tilde{D}} \quad (3)$$

where $\tilde{\varepsilon}$ is the electrical permittivity of water, \tilde{V}_T is the thermal voltage scale, $\tilde{\eta}$ is the viscosity of water and \tilde{D} is the diffusivity of dissolved ion. Note that tilde symbol (\sim) means dimensional variable, but Pe^0 is dimensionless. Assuming KCl electrolyte, the cation diffusivity and anion diffusivity is the same. The flow field, \mathbf{u} and pressure, p was governed by following dimensionless Stokes equations and continuity equation of

$$\mathbf{0} = -\nabla p + \nabla^2 \mathbf{u} \quad (4)$$

$$\text{and } \nabla \cdot \mathbf{u} = 0. \quad (5)$$

Note that Bruus's boundary model assumed extremely thin electrical double layer. Thus, in equation (4), the electrical body force term was omitted. The boundary conditions on stationary bulk were

$$c = 1, \quad \phi = V \quad \text{and} \quad p = 0 \quad (6)$$

where V is the applied voltage. On cation-selective surface,

$$\ln c + \phi = 0, \quad -\frac{\partial c}{\partial x} + c \frac{\partial \phi}{\partial x} = 0 \quad \text{and} \quad \mathbf{u} = \mathbf{0}. \quad (7)$$

Above conditions, the first one refers that electrochemical potential set to be zero. The second is zero-anion flux through cation-selective surface and third one is no-slip boundary condition. On the dielectric micropillar surfaces, the surface conduction was described by

$$\mathbf{n} \cdot (-\nabla c - c \nabla \phi) = \frac{1}{2} \mathbf{t} \cdot \nabla I^{surf} \quad (8)$$

where \mathbf{n} is the normal vector of which direction is from electrolyte to the pillar, \mathbf{t} is the tangential vector on pillar surface and I^{surf} is the surface flux of cationic species. The definition of I^{surf} can be found in [88]. We assumed highly charged micropillar surface so that the surface flux of anion was zero. This zero surface flux led to

$$\mathbf{n} \cdot (-\nabla c + c \nabla \phi) = 0. \quad (10)$$

The electroosmotic slip on micropillar surfaces was described by

$$\mathbf{u} = u_{bnd} \mathbf{t} \quad (11)$$

where the definition of u_{bnd} can be found in [88]. Equations (1) – (11) were solved by commercial finite element software, COMSOL Multiphysics.

Reference

- [1] S. J. Kim, Y.-C. Wang, J. H. Lee, H. Jang, and J. Han, "Concentration Polarization and Nonlinear Electrokinetic Flow near a Nanofluidic Channel," *Physical Review Letters*, vol. 99, no. 4, p. 044501, 2007.
- [2] T. Pundik, I. Rubinstein, and B. Zaltzman, "Bulk electroconvection in electrolyte," *Physical Review E*, vol. 72, no. 6, p. 061502, 2005.
- [3] X. Jin, S. Joseph, E. N. Gatimu, P. W. Bohn, and N. Aluru, "Induced electrokinetic transport in micro– nanofluidic interconnect devices," *Langmuir*, vol. 23, no. 26, pp. 13209–13222, 2007.
- [4] I. Rubinstein and L. Shtilman, "Voltage against current curves of cation exchange membranes," *Journal of the Chemical Society, Faraday Transactions 2: Molecular and Chemical Physics*, vol. 75, pp. 231–246, 1979.
- [5] A. Plecis, R. B. Schoch, and P. J. N. I. Renaud, "Ionic transport phenomena in nanofluidics: experimental and theoretical study of the exclusion–enrichment effect on a chip," vol. 5, no. 6, pp. 1147–1155, 2005.
- [6] P. B. Peters, R. van Roij, M. Z. Bazant, and P. M. Biesheuvel, "Analysis of electrolyte transport through charged nanopores," *Physical Review E*, vol. 93, no. 5, p. 053108, 05/13/ 2016.
- [7] S. J. Kim, L. D. Li, and J. Han, "Amplified electrokinetic response by concentration polarization near nanofluidic channel," *Langmuir*, vol. 25, no. 13, pp. 7759–7765, 2009.
- [8] G. Yossifon and H.-C. Chang, "Selection of nonequilibrium overlimiting currents: universal depletion layer formation dynamics and vortex instability," *Physical review letters*, vol. 101, no. 25, p. 254501, 2008.
- [9] S. J. Kim, Y.-A. Song, and J. Han, "Nanofluidic concentration devices for biomolecules utilizing ion concentration polarization: theory, fabrication, and applications," *Chemical Society Reviews*, 10.1039/B822556G vol. 39, no. 3, pp. 912–922, 2010.
- [10] S. Nam *et al.*, "Experimental verification of overlimiting current by surface conduction and electro–osmotic flow in microchannels," *Physical review letters*, vol. 114, no. 11, p. 114501, 2015.

- [11] E. V. Dydek, B. Zaltzman, I. Rubinstein, D. Deng, A. Mani, and M. Z. Bazant, "Overlimiting current in a microchannel," *Physical review letters*, vol. 107, no. 11, p. 118301, 2011.
- [12] I. Cho, W. Kim, J. Kim, H.-Y. Kim, H. Lee, and S. J. Kim, "Non-negligible Diffusio-osmosis inside an ion concentration polarization layer," *Physical review letters*, vol. 116, no. 25, p. 254501, 2016.
- [13] S. M. Rubinstein *et al.*, "Direct observation of a nonequilibrium electro-osmotic instability," *Physical review letters*, vol. 101, no. 23, p. 236101, 2008.
- [14] I. Rubinstein, B. Zaltzman, and I. Lerman, "Electroconvective instability in concentration polarization and nonequilibrium electro-osmotic slip," *Physical review E*, vol. 72, no. 1, p. 011505, 2005.
- [15] K. Kim, W. Kim, H. Lee, and S. J. Kim, "Stabilization of ion concentration polarization layer using micro fin structure for high-throughput applications," *Nanoscale*, vol. 9, no. 10, pp. 3466-3475, 2017.
- [16] Y. Kim and D. F. J. D. Lawler, "Overlimiting current by interactive ionic transport between space charge region and electric double layer near ion-exchange membranes," vol. 285, pp. 245-252, 2012.
- [17] M. MESBAH, U. PREMACHANDRAN, and W. B. WHITMAN, "Precise measurement of the G+ C content of deoxyribonucleic acid by high-performance liquid chromatography," *International Journal of Systematic Bacteriology*, vol. 39, no. 2, pp. 159-167, 1989.
- [18] V. Dolnik, S. Liu, and S. Jovanovich, "Capillary electrophoresis on microchip," (in eng), *Electrophoresis*, vol. 21, no. 1, pp. 41-54, Jan 2000.
- [19] B. Jung, R. Bharadwaj, and J. G. Santiago, "Thousandfold signal increase using field-amplified sample stacking for on-chip electrophoresis," (in eng), *Electrophoresis*, vol. 24, no. 19-20, pp. 3476-83, Oct 2003.
- [20] V. Neuhoff, N. Arold, D. Taube, and W. Ehrhardt, "Improved staining of proteins in polyacrylamide gels including isoelectric focusing gels with clear background at nanogram sensitivity using Coomassie Brilliant Blue G-250 and R-250," (in eng), *Electrophoresis*, vol. 9, no. 6, pp. 255-62, Jun 1988.
- [21] B. Jung, R. Bharadwaj, and J. G. Santiago, "On-chip

- millionfold sample stacking using transient isotachopheresis," (in eng), *Anal Chem*, vol. 78, no. 7, pp. 2319–27, Apr 1 2006.
- [22] K. M. Balss, W. N. Vreeland, K. W. Phinney, and D. Ross, "Simultaneous concentration and separation of enantiomers with chiral temperature gradient focusing," (in eng), *Anal Chem*, vol. 76, no. 24, pp. 7243–9, Dec 15 2004.
- [23] S. J. Kim, Y. A. Song, and J. Han, "Nanofluidic concentration devices for biomolecules utilizing ion concentration polarization: theory, fabrication, and applications," (in eng), *Chem Soc Rev*, vol. 39, no. 3, pp. 912–22, Mar 2010.
- [24] L. F. Cheow, A. Sarkar, S. Kolitz, D. Lauffenburger, and J. Han, "Detecting kinase activities from single cell lysate using concentration-enhanced mobility shift assay," (in eng), *Anal Chem*, vol. 86, no. 15, pp. 7455–62, Aug 5 2014.
- [25] H. Song, Y. Wang, C. Garson, and K. Pant, "Nafion Film Based Micro-nanofluidic Device for Concurrent DNA Preconcentration and Separation in Free Solution," (in Eng), *Microfluid Nanofluidics*, vol. 17, no. 4, pp. 693–699, Oct 1 2014.
- [26] S. H. Ko, S. J. Kim, L. F. Cheow, L. D. Li, K. H. Kang, and J. Han, "Massively parallel concentration device for multiplexed immunoassays," (in eng), *Lab Chip*, vol. 11, no. 7, pp. 1351–8, Apr 7 2011.
- [27] I. Cho, G. Y. Sung, and S. J. Kim, "Overlimiting current through ion concentration polarization layer: hydrodynamic convection effects," (in eng), *Nanoscale*, vol. 6, no. 9, pp. 4620–6, May 7 2014.
- [28] J. W. Hong, V. Studer, G. Hang, W. F. Anderson, and S. R. Quake, "A nanoliter-scale nucleic acid processor with parallel architecture," (in eng), *Nat Biotechnol*, vol. 22, no. 4, pp. 435–9, Apr 2004.
- [29] M. A. Unger, H. P. Chou, T. Thorsen, A. Scherer, and S. R. Quake, "Monolithic microfabricated valves and pumps by multilayer soft lithography," (in eng), *Science*, vol. 288, no. 5463, pp. 113–6, Apr 7 2000.
- [30] S. J. Kim, L. D. Li, and J. Han, "Amplified electrokinetic response by concentration polarization near nanofluidic channel," (in eng), *Langmuir*, vol. 25, no. 13, pp. 7759–65, Jul 7 2009.
- [31] L. F. Cheow and J. Han, "Continuous signal enhancement for

- sensitive aptamer affinity probe electrophoresis assay using electrokinetic concentration," (in eng), *Anal Chem*, vol. 83, no. 18, pp. 7086–93, Sep 15 2011.
- [32] A. A. Sonin and R. F. Probstein, "A hydrodynamic theory of desalination by electro dialysis," *Desalination*, vol. 5, no. 3, pp. 293–329, 1968.
- [33] V. V. Nikonenko *et al.*, "Intensive current transfer in membrane systems: Modelling, mechanisms and application in electro dialysis," *Advances in colloid and interface science*, vol. 160, no. 1–2, pp. 101–123, 2010.
- [34] R. Kwak, G. Guan, W. K. Peng, and J. Han, "Microscale electro dialysis: Concentration profiling and vortex visualization," *Desalination*, vol. 308, pp. 138–146, 2013.
- [35] L. Alvarado and A. Chen, "Electrodeionization: principles, strategies and applications," *Electrochimica Acta*, vol. 132, pp. 583–597, 2014.
- [36] J.-H. Han, E. Khoo, P. Bai, and M. Z. Bazant, "Over-limiting current and control of dendritic growth by surface conduction in nanopores," *Scientific reports*, vol. 4, p. 7056, 2014.
- [37] S. J. Kim, S. H. Ko, K. H. Kang, and J. Han, "Direct seawater desalination by ion concentration polarization," *Nature Nanotechnology*, vol. 5, no. 4, p. 297, 2010.
- [38] D. Deng, W. Aouad, W. A. Braff, S. Schlumpberger, M. E. Suss, and M. Z. Bazant, "Water purification by shock electro dialysis: Deionization, filtration, separation, and disinfection," *Desalination*, vol. 357, pp. 77–83, 2015.
- [39] B. Kim *et al.*, "Purification of high salinity brine by multi-stage ion concentration polarization desalination," *Scientific reports*, vol. 6, p. 31850, 2016.
- [40] S. Park *et al.*, "Capillarity ion concentration polarization as spontaneous desalting mechanism," *Nature communications*, vol. 7, p. 11223, 2016.
- [41] H. Strathmann, "Electro dialysis, a mature technology with a multitude of new applications," *Desalination*, vol. 264, no. 3, pp. 268–288, 2010.
- [42] M. Tedesco, H. Hamelers, and P. Biesheuvel, "Nernst-Planck transport theory for (reverse) electro dialysis: I. Effect of co-ion transport through the membranes," *Journal of Membrane Science*, vol. 510, pp. 370–381, 2016.
- [43] J. Balster, D. Stamatialis, and M. Wessling, "Membrane with

- integrated spacer," *Journal of membrane science*, vol. 360, no. 1-2, pp. 185-189, 2010.
- [44] B. Kim, S. Choi, V. S. Pham, R. Kwak, and J. Han, "Energy efficiency enhancement of electromembrane desalination systems by local flow redistribution optimized for the asymmetry of cation/anion diffusivity," *Journal of Membrane Science*, vol. 524, pp. 280-287, 2017.
- [45] O. Kedem and Y. Maoz, "Ion conducting spacer for improved ED," *Desalination*, vol. 19, no. 1-3, pp. 465-470, 1976.
- [46] P. Długołęcki, J. Dąbrowska, K. Nijmeijer, and M. Wessling, "Ion conductive spacers for increased power generation in reverse electrodialysis," *Journal of membrane science*, vol. 347, no. 1-2, pp. 101-107, 2010.
- [47] V. K. Shahi, S. Thampy, and R. Rangarajan, "The effect of conducting spacers on transport properties of ion-exchange membranes in electrodriven separation," *Desalination*, vol. 133, no. 3, pp. 245-258, 2001.
- [48] J. Balster, I. Pünt, D. Stamatialis, and M. Wessling, "Multi-layer spacer geometries with improved mass transport," *Journal of membrane science*, vol. 282, no. 1-2, pp. 351-361, 2006.
- [49] A. A. Sonin and M. S. Isaacson, "Optimization of flow design in forced flow electrochemical systems, with special application to electrodialysis," *Industrial & Engineering Chemistry Process Design and Development*, vol. 13, no. 3, pp. 241-248, 1974.
- [50] G. Yossifon, P. Mushenheim, and H.-C. Chang, "Controlling nanoslot overlimiting current with the depth of a connecting microchamber," *EPL (Europhysics Letters)*, vol. 90, no. 6, p. 64004, 2010.
- [51] S. Sohn, I. Cho, S. Kwon, H. Lee, and S. J. Kim, "Surface conduction in a microchannel," *Langmuir*, vol. 34, no. 26, pp. 7916-7921, 2018.
- [52] C. P. Nielsen and H. Bruus, "Concentration polarization, surface currents, and bulk advection in a microchannel," *Physical Review E*, vol. 90, no. 4, p. 043020, 2014.
- [53] A. Yaroshchuk, "A. Yaroshchuk, E. Zholkovskiy, S. Pogodin, and V. Baulin, *Langmuir* 27, 11710 (2011)," *Langmuir*, vol. 27, p. 11710, 2011.
- [54] S. J. Kim, S. H. Ko, R. Kwak, J. D. Posner, K. H. Kang, and J.

- Han, "Multi-vortical flow inducing electrokinetic instability in ion concentration polarization layer," *Nanoscale*, vol. 4, no. 23, pp. 7406–7410, 2012.
- [55] B. D. Storey, B. Zaltzman, and I. Rubinstein, "Bulk electroconvective instability at high Peclet numbers," *Physical Review E*, vol. 76, no. 4, p. 041501, 2007.
- [56] J. D. Posner and J. G. Santiago, "Convective instability of electrokinetic flows in a cross-shaped microchannel," *Journal of Fluid Mechanics*, vol. 555, pp. 1–42, 2006.
- [57] S. M. Davidson, M. B. Andersen, and A. Mani, "Chaotic induced-charge electro-osmosis," *Physical review letters*, vol. 112, no. 12, p. 128302, 2014.
- [58] C.-H. Chen, H. Lin, S. K. Lele, and J. G. Santiago, "Convective and absolute electrokinetic instability with conductivity gradients," *Journal of Fluid Mechanics*, vol. 524, pp. 263–303, 2005.
- [59] J. Kim, I. Cho, H. Lee, and S. J. Kim, "Ion Concentration Polarization by Bifurcated Current Path," *Scientific Reports*, vol. 7, no. 1, p. 5091, 2017/07/11 2017.
- [60] D. Deng *et al.*, "Overlimiting current and shock electro dialysis in porous media," *Langmuir*, vol. 29, no. 52, pp. 16167–16177, 2013.
- [61] R. B. Schoch, J. Han, and P. Renaud, "Transport phenomena in nanofluidics," *Reviews of modern physics*, vol. 80, no. 3, p. 839, 2008.
- [62] Q. Pu, J. Yun, H. Temkin, and S. Liu, "Ion-enrichment and ion-depletion effect of nanochannel structures," *Nano letters*, vol. 4, no. 6, pp. 1099–1103, 2004.
- [63] S.-H. Lee *et al.*, "Sub-10 nm transparent all-around-gated ambipolar ionic field effect transistor," *Nanoscale*, vol. 7, no. 3, pp. 936–946, 2015.
- [64] K. Lee, H. Lee, S.-H. Lee, H.-M. Kim, K.-B. Kim, and S. J. Kim, "Enhancing the sensitivity of DNA detection by structurally modified solid-state nanopore," *Nanoscale*, vol. 9, no. 45, pp. 18012–18021, 2017.
- [65] B. J. Kirby and E. F. Hasselbrink Jr, "Zeta potential of microfluidic substrates: 1. Theory, experimental techniques, and effects on separations," *Electrophoresis*, vol. 25, no. 2, pp. 187–202, 2004.
- [66] A. Revil and P. W. J. Glover, "Theory of ionic-surface electrical conduction in porous media," *Physical Review B*,

- vol. 55, no. 3, pp. 1757–1773, 01/15/ 1997.
- [67] J. Kim, H.-Y. Kim, H. Lee, and S. J. Kim, "Pseudo 1-D Micro/Nanofluidic Device for Exact Electrokinetic Responses," *Langmuir*, vol. 32, no. 25, pp. 6478–6485, 2016.
- [68] D. F. Blair, "How bacteria sense and swim," *Annual Reviews in Microbiology*, vol. 49, no. 1, pp. 489–520, 1995.
- [69] G. H. Wadhams and J. P. Armitage, "Making sense of it all: bacterial chemotaxis," *Nature Reviews Molecular Cell Biology*, vol. 5, no. 12, pp. 1024–1037, 2004.
- [70] I. B. Zhulin, E. H. Rowsell, M. S. Johnson, and B. L. Taylor, "Glycerol elicits energy taxis of Escherichia coli and Salmonella typhimurium," *Journal of bacteriology*, vol. 179, no. 10, pp. 3196–3201, 1997.
- [71] J. Zhuang *et al.*, "Analytical modeling and experimental characterization of chemotaxis in *Serratia marcescens*," *Physical Review E*, vol. 89, no. 5, p. 052704, 2014.
- [72] J. J. Min, V. H. Nguyen, H. J. Kim, Y. Hong, and H. E. Choy, "Quantitative bioluminescence imaging of tumor-targeting bacteria in living animals," *Nat Protoc*, vol. 3, no. 4, pp. 629–36, 2008.
- [73] E. Choi, H.-k. Chang, C. Young Lim, T. Kim, and J. Park, "Concentration gradient generation of multiple chemicals using spatially controlled self-assembly of particles in microchannels," *Lab on a Chip*, 10.1039/C2LC40450H vol. 12, no. 20, pp. 3968–3975, 2012.
- [74] S. J. Park *et al.*, "New paradigm for tumor theranostic methodology using bacteria-based microrobot," *Scientific reports*, vol. 3, 2013.
- [75] M. Eisenbach, "Control of bacterial chemotaxis," *Mol Microbiol*, vol. 20, no. 5, pp. 903–10, Jun 1996.
- [76] B. Behkam and M. Sitti, "Bacterial flagella-based propulsion and on/off motion control of microscale objects," *Applied Physics Letters*, vol. 90, no. 2, pp. –, 2007.
- [77] D. Kim, A. Liu, E. Diller, and M. Sitti, "Chemotactic steering of bacteria propelled microbeads," (in English), *Biomedical Microdevices*, vol. 14, no. 6, pp. 1009–1017, 2012/12/01 2012.
- [78] K. Nogawa, M. Kojima, M. Nakajima, M. Homma, F. Arai, and T. Fukuda, "Smart manipulation of multiple bacteria-driven microobjects based on bacterial autonomous movement," in *Intelligent Robots and Systems (IROS), 2011*

- IEEE/RSJ International Conference on*, 2011, pp. 1693–1698.
- [79] S. J. Park *et al.*, "New paradigm for tumor theranostic methodology using bacteria-based microrobot," *Sci. Rep.*, Article vol. 3, 12/02/online 2013.
- [80] A. Sahari, D. Headen, and B. Behkam, "Effect of body shape on the motile behavior of bacteria-powered swimming microrobots (BacteriaBots)," *Biomed Microdevices*, vol. 14, no. 6, pp. 999–1007, Dec 2012.
- [81] B. Behkam and M. Sitti, "Characterization of bacterial actuation of micro-objects," in *Robotics and Automation, 2009. ICRA'09. IEEE International Conference on*, 2009, pp. 1022–1027: IEEE.
- [82] B. S. Edward, S. Mahmut Selman, K. Dal Hyung, K. Vijay, J. P. George, and K. Min Jun, "Electrokinetic and optical control of bacterial microrobots," *Journal of Micromechanics and Microengineering*, vol. 21, no. 3, p. 035001, 2011.
- [83] S. J. Park, H. Bae, J. Kim, B. Lim, J. Park, and S. Park, "Motility enhancement of bacteria actuated microstructures using selective bacteria adhesion," *Lab on a Chip*, 10.1039/C000463D vol. 10, no. 13, pp. 1706–1711, 2010.
- [84] I. Rubinstein and B. Zaltzman, "Electro-osmotically induced convection at a permselective membrane," *Physical Review E*, vol. 62, no. 2, p. 2238, 2000.
- [85] J. H. Masliyah and S. Bhattacharjee, *Electrokinetic and colloid transport phenomena*. John Wiley & Sons, 2006.
- [86] B. J. Kirby and E. F. Hasselbrink, "Zeta potential of microfluidic substrates: 2. Data for polymers," *Electrophoresis*, vol. 25, no. 2, pp. 203–213, 2004.
- [87] R. F. Probstein, *Physicochemical hydrodynamics: an introduction*. John Wiley & Sons, 2005.
- [88] C. P. Nielsen and H. Bruus, "Concentration polarization, surface currents, and bulk advection in a microchannel," *Physical Review E*, vol. 90, p. 043020, 2014.

초 록

이온 선택성은 나노 유체 채널의 독특한 특성 중 하나입니다. 나노 채널 두께에 비해, Debye 층 길이 두께는 무시할 수 없으므로 특정 조건 하에서 나노 채널 내부에서 전기 이중층이 중첩됩니다. 전압이 마이크로 나노 채널을 통해 인가됨에 따라 이온 농도 분극 현상이 나타난다. ICP의 메커니즘은 DC 전압을 인가하여 주면 막과 동일한 극성의 이온은 나노막을 통과하지 못하고, 막과 반대 극성의 이온만이 나노막을 통과하게 되어 막의 양극 및 음극 측에서 이온 농도의 불균형을 만든다. 나노막 양단에 전해질 농도가 급격히 낮아지는 이온 공핍 영역과 높아지는 영역 이온 부유 영역으로 분극이 일어나게 되어 이를 이온 농도 분극 현상이라고 한다. 공핍 영역의 ICP에 의한 이온 분포는 2 개의 영역으로 나눌 수 있다. 이온 공핍 영역 내부에서는 전기 삼투 불안정성(유동이 매우 불안정), 과한계 전류 등 다양한 근본적인 문제가 연구되어왔다. 공핍 영역 밖에서는 유체의 연속적으로 추출할 수 있어 정화 / 해수의 담수화 / 농축에

응용할 수 있어 중요한 관심을 끌고 있다. 본 논문에서는 마이크로 채널의 기하학적 구조를 변화시키고 미세 구조물들을 설치함으로써 이온 농도 분극 현상에 공핍 영역 내부와 외부의 전기동역학적 반응을 실험적으로 검증하였다. 전기동역학적 반응을 검증하기 위해 농도 프로파일, 입자 추적 및 전기적 현상을 검증한다. 논문은 총 4 장으로 나누어져 있다.

2 장에서 이온 농도 분극 현상을 기반으로 물리 화학적 성질 다른 전하를 띤 입자들의 선택적 농축, 분리 및 압출을 위한 다중층 마이크로 / 나노수력학 장치를 제안한다. 전기 삼투 마찰힘과 전기 영동 힘의 균형을 통해, 이들은 높은 농도로 농축과 동시에 분리 될 수 있다. 반복된 마이크로 챔버 구조의 설계로 인해 이온 공핍 영역이 안정화 되었고 플러그가 잘 관찰된다. 온칩 또는 오프 칩 적용을 위해 공압 마이크로 밸브를 시스템에 결합하여 선택적으로 압출할 수 있다. 이러한 통합 시스템을 이용해서, 알렉사 염료는 추가 확산이나 분산없이 Sulforhodamine B와 Alexa Fluor 488의 혼합물로부터 압출할 수 있다,

두번째로, 3 장에서는 멀티시뮬레이션과 마이크로 / 나노 유체 실험에 의해 마이크로 갭힌 공간에서 마이크로 유전체 필라 구조물의 전기동역학적 효과를 보고자 제안했다. 선택 투과성 막으로 구성된 매크로 시스템의 유전체 마이크로 구조물들은 전류가림효과로 인해 이온 전달에 부정적인 영향을 미친다. 하지만, 이온 수송의 주요 구동 메커니즘을 전기불안정유동(EOI)에서 표면 전도(SC) 및 전기 삼투 유동(EOF)으로 전환함에 따라 마이크로 스케일 한정 시스템에서는 이온 수송을 촉진시킬 수 있게 된다. 이 장에서는 마이크로 유전체 필라 구조물에 SC와 EOF가 다중 시뮬레이션과 실험을 통한 가시화로, 이온 수송을 촉진할 수 있는 이유에 대해 정확한 증거를 보여준다. 추가 이온 부유 영역은 이온 공핍 영역 내부의 마이크로 유전체 필라 구조물에 형성되어 추가 이온 부유 영역이 대량의 이온들을 나노 다공성 막에 직접 연결할 수 있다. 또한 그 동안 중요하게 여겨지지 않은 구조물의 배치, 즉 마이크로 필라 배열이 SC와 EOF에 어떻게 중요한 영향을 미치는지 확인한다. EOF에 의해 staggerd 형태 필라 구조물은 와류가 격리되어 있게 되고, aligned 형태 필라 구조물은

와류가 전체적으로 이어져 있다. 이것은 결국 aligned 형태 필라 구조물이 보다 효율적인 이온 전달을 할 수 있으며, 결국 높은 과한계 전류로 이어지게 된다.

셋째, 4 장에서 이온 공핍 영역 내에서 서로 다른 스페이서 구조물들을 사용하여 거시적 시스템에서의 이온 전달 향상에 대한 실험적 및 다중 시뮬레이션을 제안한다. 두 가지 다른 스페이서 구조물로 농도분포와 전기적현상을 통해 우리는 특정 패턴화된 스페이서 구조는 원하지 않는 곳에서는 전기불안정유동을 억제하고 원하는 곳에서는 전기 대류 혼합을 고정시킴으로서 이온 전달을 보다 효과적으로 할 수 있다. 적절히 패턴화된 구조물로 의해, 우리는 전기대류성 와류를 조정할 수 있고 전기 전도성 혼합 효율을 향상시킬 수 있었다.

논문 주제와 관련이 없기 때문에 부록 A는 주요 장에서 제외되었다. 부록 A에서 층류 특성을 이용하여, 마이크파티클에 *S. typhimurium* 박테리아를 이방성 부착하고 주화성을 입증하였다. 위아래로 유동흐름을 제어하여 박테리아의 이방성 부착을 가능하게

하였다. 형광 세기 와 SEM 이미징을 통해 직접 시각화하여
검증하였다. 부록 B와 C는 각각 2 장과 3 장에 대한 수치 해석이다.

Key words: 마이크로/나노, 전기동역학, 선택적 이온전달,
이온농도분극현상, 과한계전류, 농축. 유전체 필라, 스페이서

Student number: 2013-23145